Remote Sensing of Environment 147 (2014) 23–42

Contents lists available at ScienceDirect

Remote Sensing of Environment

journal homepage: www.elsevier.com/locate/rse

Impacts of the broadband albedo on actual evapotranspiration estimated by S-SEBI model over an agricultural area

C. Mattar [a,b,*], B. Franch [c,d], J.A. Sobrino [a], C. Corbari [e], J.C. Jiménez-Muñoz [a], L. Olivera-Guerra [b], D. Skokovic [a], G. Sória [a], R. Oltra-Carriò [a], Y. Julien [a], M. Mancini [e]

[a] Global Change Unit, Image Processing Laboratory, University of Valencia Science Park, C/Catedrático José Beltrán 2, 46980 Paterna, Valencia, Spain
[b] Laboratory for Analysis of the Biosphere (L.A.B.), University of Chile, Av. Santa Rosa 11315, La Pintana, Santiago, Chile
[c] Department of Geographical Sciences, University of Maryland, College Park, MD 20742, United States
[d] NASA Goddard Space Flight Center, 8800 Greenbelt Road, Greenbelt, MD 20771, United States
[e] Department of Civil and Environmental Engineering, Politecnico di Milano, Piazza Leonardo da Vinci, 32, Milan, Italy

ARTICLE INFO

Article history:
Received 11 May 2013
Received in revised form 17 February 2014
Accepted 20 February 2014
Available online 12 March 2014

Keywords:
Surface broadband albedo
BRDF
AHS
Angular variation
Heat fluxes
Evapotranspiration
S-SEBI

ABSTRACT

Surface albedo and emissivity are essential variables in surface energy balance. In recent decades, several land surface energy models have used both surface broadband albedo and emissivity in order to achieve reliable evapotranspiration retrievals on a daily basis. Despite these improvements in surface energy models, we noticed an assumption that most studies make when using this framework. It assumes that the surface broadband albedo and emissivity can be estimated directly as a weighted average of spectral surface bi-directional reflectances, and as a weighted average of spectral surface emissivities retrieved at a given view angle, respectively. However, this approach does not take into account surface anisotropy, which is described by the Bi-directional Reflectance Distribution Function (BRDF) in the case of the surface albedo. In this paper, we analyze the influence that estimating land surface albedo directly from the surface reflectance (α_{REF}) or through the BRDF integration (α_{BRDF}) has on the estimation of energy balance components (net radiation, latent and sensible heat fluxes and evapotranspiration) by using the Simplified Surface Energy Balance Index (S-SEBI). To this end, in-situ data and remote sensing images acquisitioned at different view zenith angles (VZA) such as 0°, ±40° and ±57° by the Airborne Hyperspectral Scanner (AHS) over an agricultural area were used. Results show high variation in α_{REF} depending on the VZA when compared to α_{BRDF}, with the highest difference observed in the backward scattering direction along the hot spot region (RMSE of 0.11 and relative error of 65%). Net radiation gives relative errors from 6 to 17%, with the maximum error obtained in the images that include the hot spot effect, whereas significant changes are not observed in case of the ground heat flux and the evaporative fraction. However, sensible heat flux, latent heat flux and daily evapotranspiration show relative errors ranging between 23–39%, 6–18% and 5–15% respectively. In a future study, the influence of estimating surface emissivity directly from the average of spectral emissivities under a given view angle or using a hemispherical value will be analyzed.

1. Introduction

Surface albedo is a key radiation parameter required for modeling the Earth's energy budget and land–atmosphere radiative interactions. It is a crucial parameter in determining the magnitude of energy fluxes in the soil–plant–atmosphere continuum (Bonan, 2008; Chapin, Randerson, McGuire, Foley, & Field, 2008) as it affects surface temperature, evaporation and transpiration, cloud formation and precipitation, thus ultimately impacting gross primary productivity (Dickinson, 1983; Lawrence & Slingo, 2004; Ollinger et al., 2008; Sellers et al., 1997).

Theoretically, surface albedo is defined as the ratio between the upwelling and down-welling incident irradiance upon a surface. While surface reflectance is defined as this same fraction for a single incident angle, albedo is the directional integration of reflectance over all sun-view geometries (Pinty & Verstraete, 1992). Thus, the estimation of surface albedo is based on different angular measurements of surface reflectance. The Bidirectional Reflectance Distribution Function (BRDF) describes the directional dependence of land reflectance as a function of the sun-target-sensor geometry. Therefore, surface albedo is derived by integrating a BRDF model over all view and illumination angles. Consequently, a high number of angular measurements are required to calculate surface albedo.

Surface albedo is estimated from ground-based measurements using albedometers or through several directional surface reflectance measurements using a goniometric system (Liang, Li, & Wang, 2012). These measurements, however, are very time consuming and only few surfaces can be characterized and measured. Given this, and

* Corresponding author.
E-mail address: cristian.mattar@uv.es (C. Mattar).

http://dx.doi.org/10.1016/j.rse.2014.02.011
0034-4257/

in order to account for a wide range surface cover types, remote sensing fulfills an important role in obtaining accurate retrievals of surface albedo. However, in some cases the estimation of surface albedo from remotely sensed data (mostly when working with airborne data) is a challenging problem due to low angular sampling. Several authors have reported relevant results obtained from surface albedo estimations made from satellite observations, such as the Moderate Resolution Imaging Spectroradiometer (MODIS), the Advanced Very High Resolution Radiometer (AVHRR), the POLarization and Directionality of the Earth's Reflectances (POLDER), the Multi-angle Imaging Spectroradiometer (MISR) and the Spinning Enhanced Visible and InfraRed Imager (SEVIRI) (Diner, 1999; Geiger, Carrer, Franchisteguy, Roujean, & Meurey, 2008; He et al., 2012; Leroy et al., 1997; Pinty et al., 2000; Pinty et al., 2011; Schaaf et al., 2002; Strugnell & Lucht, 2001) Moreover, those estimations have been widely validated with ground measurements across several types of land cover (Cescatti et al., 2012; Chen, Liang, Wang, Kim, & Martonchik, 2008; Jin, Schaaf, Gao, et al., 2003; Jin, Schaaf, Woodcock, et al., 2003; Liang et al., 2002; Liu et al., 2009; Román et al., 2009, 2010; Wang, Liang, Schaaf, & Strahler, 2010).

Detailed knowledge of land surface fluxes, especially latent and sensible heat components, is important for monitoring land surface processes in weather and climate models that predict fluxes exchanges between the surface and the lower atmosphere, and for agricultural applications such as irrigation scheduling (Courault, Seguin, & Olioso, 2005; Kalma, McVicar, & McCabe, 2008). In fact, a sensitivity analysis estimating the impact of albedo uncertainties on climate modeling showed that absolute albedo accuracy of between ± 0.02 and ± 0.03, equivalent to an uncertainty of $\pm 10\ \mathrm{Wm}^{-2}$ of the net radiation, results in significant changes in regional climate simulations (Nobre, Sellers, & Shukla, 1991; Sellers et al., 1995).

One of the key factors behind the land surface energy process is evapotranspiration (*ET*). This is defined as the flux of water evaporated at the earth–atmosphere interface (from soil, water bodies and interception) and transpired by vegetation through stomata in its leaves as a consequence of photosynthetic processes. Surface albedo accuracy must directly affect the precision of the net radiation and thus, indirectly, the daily evapotranspiration and other land surface fluxes. Nevertheless, no focused research analyzing the impact of albedo accuracy on surface energy balance parameters has been done yet. Basically, in the case of evapotranspiration models (Allen, Tasumi, & Trezza, 2007; Bastiaanssen, Menenti, Feddes, & Holtslag, 1998; Corbari, Ravazzani, & Mancini, 2011; Menenti & Choudhury, 1993; Roerink, Su, & Menenti, 2000; Su, 2002), when there are no in-situ data available, the surface albedo can be estimated in different ways. Most studies, however, assume the surface to be Lambertian, thus considering the albedo to be equivalent to surface reflectance (French et al., 2005; Galleguillos, Jacob, Prévot, French, & Lagacherie, 2011; McCabe & Wood, 2006; Sobrino, Gomez, et al., 2007; Timmermans, Kustas, Anderson, & French, 2007; Tittebrand & Berger, 2008; Verstraeten, Veroustraete, & Feyen, 2005; Vinukollu, Wood, Ferguson, & Fisher, 2011). All these works showed significant and relevant statistical results with regard to the performance of the evapotranspiration model and show no error sensibility of the influence of albedo accuracy on the results.

With a focus on the important role that surface albedo has on land surface fluxes, the main objective of this work is to evaluate the impact that considering surface broadband albedo derived from the BRDF to have the same magnitude derived from the surface reflectance has on energy balance components, especially on the estimation of daily evapotranspiration. To this end, the paper is structured as follows: Section 2 provides the data set and study area. Section 3 describes the methodology used to estimate the surface energy components, comparison and evapotranspiration methods. Section 4 presents the results obtained in this work and the following sections include a brief discussion and conclusions of this study.

2. Study area and data acquisition

2.1. Barrax test site

The study area of Barrax is located in the La Mancha region of Spain (Fig. 1). This test site is in the western part of the province of Albacete, 28 km from the capital town of Albacete (39°3′N, 2°60′W). The surface cover of the study area includes annual crops and natural surfaces such as alfalfa, wheat, oat, corn, green grass and bare soil. A detailed description of Barrax test site is presented in Sobrino, Mattar, Gastellu-Etchegorry, Jiménez-Muñoz, and Grau (2011).

The Barrax test site is one of the most important calibration/validation areas widely used for field campaigns in Europe. A complete overview of some field campaigns and their applications are detailed in Sobrino et al. (2008, 2009, 2013); Sobrino, Franch, Oltra-Carrió, Vermote, and Fedele (2013); Sobrino, Franch, Mattar, Jiménez-Muñoz, and Corbari (2012). This paper is focused on the field campaign developed in the framework of the Earth Observation: Optical Data Calibration and Information eXtraction (EODIX) project. It was carried out from the 10th to the 12th of June 2011, when extensive in-situ and airborne measurements were carried out over several crops and natural areas. The two data types are described as follows.

2.2. In-situ data

2.2.1. Continuous measurements

During the EODIX field campaign, two fixed meteorological and flux stations complemented with radiometric measurements were placed in two different crops: wheat and barley fields.

In the case of the wheat field, air temperature, relative air humidity, net radiation and ground heat flux were acquired at a time step of 10 min. Net radiation was measured using two different automatic pyranometer and pyrgeometer instruments (NR01-L4) which collected the down and up-welling radiance in the short and thermal infrared range. Ground heat flux was measured by the integration of two heat plates installed at two different soil depths (5 and 10 cm). Finally, air temperature and relative humidity were measured by single instrument (HMP45C-L).

Over the barley crop, an eddy covariance tower was installed. Latent and sensible heat fluxes were measured by a three-dimensional sonic anemometer (Young 81000) and open path gas analyzer (LICOR 7500) located at the top of a 5 meter tower. Data were collected at high frequency (20 Hz) and then averaged each minute. Energy fluxes were initially corrected by applying instrumental and physical corrections (Corbari, Masseroni, & Mancini, 2012). In particular, the Webb correction for density fluctuations (Webb, Pearman, & Leuning, 1980) and the correction for buoyancy flux due to sonic temperature measurements (Liu, Peters, & Foken, 2001) were considered. In addition, tilt correction was applied (Tanner & Thurtell, 1969). Frequency response corrections (Massman and Lee, 2002) and despiking procedure were also applied. Net radiation, relative air humidity and air temperature were measured at a 1 minute time step.

2.2.2. Transects

In-situ measurements for calibration and validation purposes were carried out simultaneously with the airborne overpass. Biogeophysical parameters such as land surface emissivity and temperature, in addition to visible and near-infrared surface reflectance, were retrieved by transects over different surface types of the test area in order to obtain sufficient representative spectra. The Thermal Infra-Red (TIR) measurements (emissivity and LST) were carried out using a CIMEL CE312-2 radiometer. The CIMEL CE312-2 is a radiance-based thermal-infrared radiometer composed of an optical head and a data storage unit. Its detector includes 6 bands, a broadband, 8–13 μm, and five narrower filters, 8.1–8.5 μm, 8.5–8.9 μm, 8.9–9.3 μm, 10.3–11 μm and 11–11.7 μm. The emissivity characterization of different

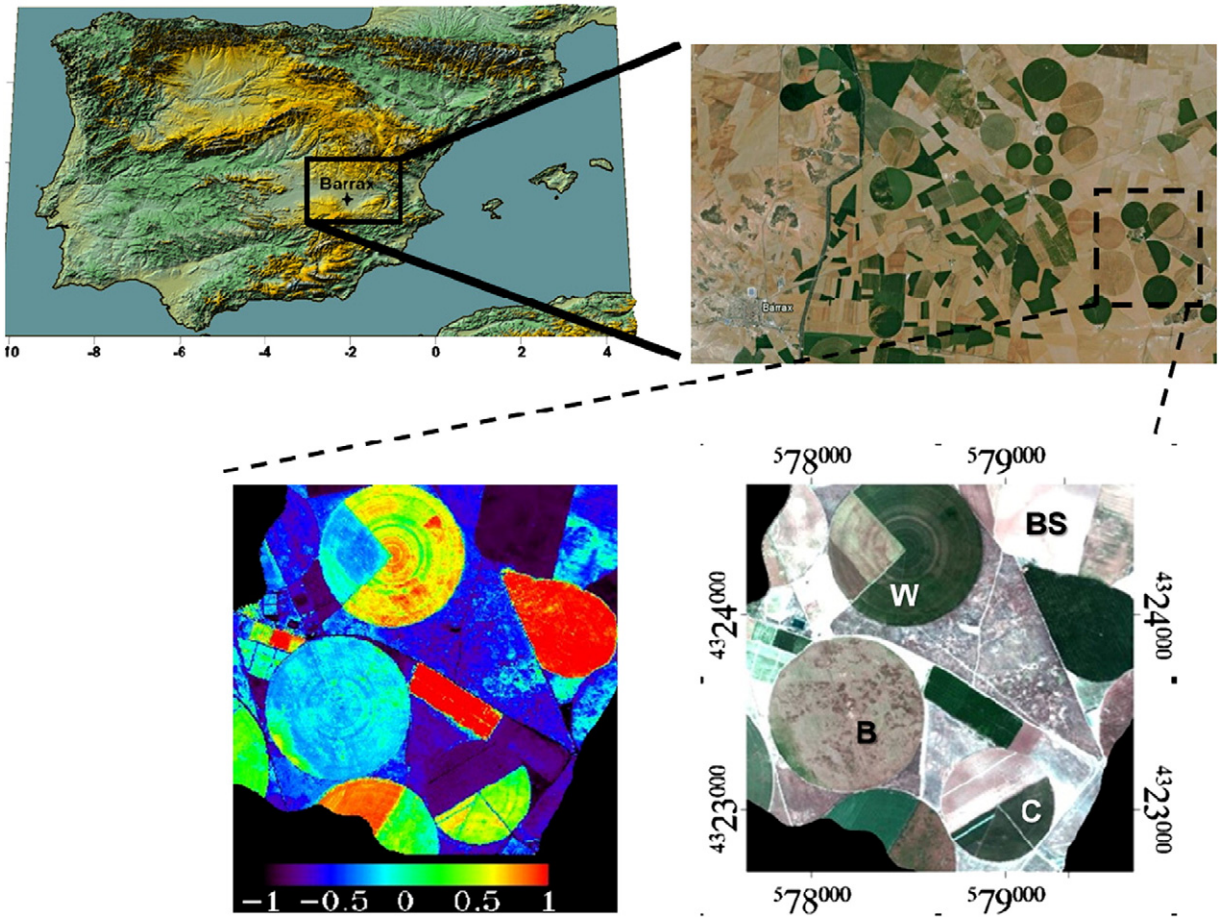

Fig. 1. The study area of Barrax, Spain. Different cover types such as Barley (B), Wheat (W), Corn (C) and Bare soil (BS) are shown. The Normalized Difference Vegetation Index (NDVI) is also presented.

surfaces was carried out by means of the TES (Temperature and Emissivity Separation) algorithm (Gillespie, Rokugawa, Matsunaga, Cothern, Hook, & Khale, 1998) applied to ground-based measurements (Jiménez-Muñoz and Sobrino, 2006; Payan and Royer, 2004; Sobrino et al., 2009, 2011).

Regarding the Visible and Near Infrared (VNIR) measurements, transects were carried out using an ASD Field Spec 3 spectroradiometer and, in addition, we had at our disposal a GER-1500 spectroradiometer mounted in a goniometer system. These latter measurements were carried out in a corn field in order to validate both the surface reflectance and the albedo derived from AHS imagery. More details on these measurements can be found in Sobrino et al. (2013).

2.3. Airborne data

The airborne data studied in this work were acquired by the Airborne Hyperspectral Scanner (AHS), which is an 80-band airborne imaging radiometer, developed and built by SensyTech Inc., (currently Argon ST, and formerly Aedalus Ent. Inc.), and operated by the Spanish Institute for Aerospace Technology (INTA). It has 63 bands in the reflective part of the electromagnetic spectrum, 7 bands in the 3 to 5 μm range and 10 bands in the 8 to 13 micron region. The AHS was installed in a CASA-212 200 *paternina* Series aircraft, and integrated with a GPS/INS POS-AV 410 from Applanix.

The data used in this work were acquired in straight line at an altitude of 2545 m above sea level on the 12th of June, 2011. The resulting data have a ground spatial resolution of 4 m. During this campaign, several flights were carried out from 9 to 10 UTC in order to obtain enough bidirectional observations to retrieve the BRDF of the test area and to estimate the surface reflectance in the VNIR spectral range. Fig. 2 shows the flight lines followed. They were planned bearing in mind the symmetry of the BRDF in the orthogonal plane. In order to achieve view zenith angles near 60°, a wedge was placed under the AHS, thereby tilting the sensor during the flights carried out along the furthest flight lines with regard to the main area. To conclude, Table 1 summarizes the whole data used in this work.

3. Methods

3.1. Atmospheric correction

During the EODIX field campaign, seven flight overpasses were processed. These images belong to different wavelengths between the visible and the thermal infrared. Thus, two different corrections were carried out in order to obtain the surface reflectance and albedo respectively from VNIR data, and land surface temperature and emissivity from TIR data.

Airborne images from the visible and near infrared spectral range were atmospherically corrected with the radiative transfer code 6S (Vermote, Tanré, Deuzé, Herman, & Morcrette, 1997) and assuming a Lambertian surface (Franch, Vermote, Sobrino, & Fédèle, 2013). The necessary inputs in this process were the aerosol optical thickness at 550 nm (which was retrieved continuously during the campaign with a CE318 sunphotometer), the water vapor content (determined from a local radiosounding performed simultaneously to the airborne overpass), as well as the geometrical conditions of each pixel of each image (day of the year, solar zenith angle, view zenith angle and relative azimuth angle). Surface reflectance images resulting from the atmospheric correction scheme were tested with

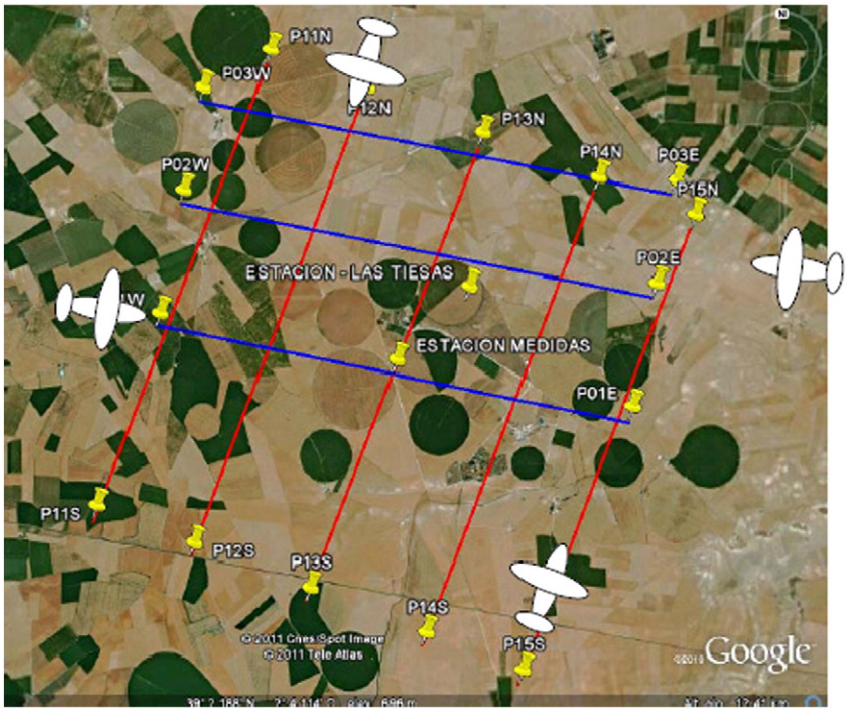

Fig. 2. Flight lines over the test area on 12th June.

in-situ measurements retrieved by an ASD spectroradiometer providing a RMSE under 0.03 for each band. Additional information about the validation process can be found in Sobrino et al. (2013).

Otherwise, thermal correction was carried out using the Modtran atmospheric radiative code (Berk et al., 1999) and vertical atmospheric profile data derived from an in-situ radiosonde launching during each flight over pass, as presented in Sobrino, Jiménez-Muñoz, Zarco-Tejada, Sepulcre-Cantó, and de Miguel (2006).

3.2. Albedo estimations

Surface reflectance is highly anisotropic. For a given sun angle, surface reflectance may vary by a factor of two in the near infrared and even more in the visible part of the electromagnetic spectrum (Kriebel, 1978). The largest reflectance variations are observed close to the backscattering direction, which is seldom observed by cross-track sensors (Breon, Maignan, Leroy, & Grant, 2002; Vermote & Roy, 2002). Nevertheless, even when this particular viewing geometry is avoided, the reflectance variations due to observation geometry can be of the same order as the temporal variations (Roy, Lewis, & Justice, 2002).

As discussed in the introduction, BRDF describes the directional dependence of land reflectance as a function of sun-target-sensor geometry. In this paper, we use the RossThick-LiSparse-Reciprocal BRDF model (Strahler et al., 1999) but corrected for the Hot-Spot process proposed by Maignan, Breon, and Lacaze (2004). The theoretical basis for this semi-empirical model is that land surface reflectance is modeled as a sum of three kernels (1) representing basic scattering types: isotropic scattering, radiative transfer-type volumetric scattering, such as from horizontally homogeneous leaf canopies, and geometric–optical surface scattering, such as from scenes containing three-dimensional objects that cast shadows and are mutually obscured from view at off-nadir angles.

$$\rho(\theta_s, \theta_v, \phi) = k_0 + k_1 F_1(\theta_s, \theta_v, \phi) + k_2 F_2(\theta_s, \theta_v, \phi) \quad (1)$$

Where θ_s is the sun zenith angle, θ_v is the view zenith angle, φ is the relative azimuth angle, F_1 is the volume scattering kernel, based on the Rossthick function derived by Roujean, Leroy, and Deschamps (1992) but corrected for the Hot-Spot process proposed by Maignan et al. (2004) and F_2 is the geometric kernel, based on the LiSparse-Reciprocal model (Li & Strahler, 1992) but using the reciprocal form given by Lucht (1998). F_1 and F_2 are fixed functions of the observation geometry and k_0, k_1, and k_2 are the model parameters associated with each kernel, which are free parameters.

BRDF has been shown to be significantly different for bare soil and vegetated surfaces because vegetated surfaces show higher anisotropy than bare soil does. More specific, over vegetation targets, directional signatures are characterized by a strong increase toward backscattering

Table 1
Data set used in this work retrieved during EODIX field campaign.

Type	Coordinates	Land cover	Measurement
Meteorological and flux tower	39° 3′ 46.4″ N 2° 5′ 33.8″ W	Wheat	Net radiation, air temperature, relative humidity, soil moisture, ground flux
Meteorological and flux tower	39° 03′ 17.3″ N 2° 05′ 38.9″ W	Barley	Net radiation, air temperature, relative humidity, soil moisture, ground flux, Latent and Sensible heat fluxes
Land Leaving Radiance (transects)	Different locations	Bare soil, alfalfa, corn, barley, wheat and green grass	Spectral signature (visible and near infrared) Land surface temperature and emissivity (narrow thermal bands)
Airborne	39° 4′ 1.6″ N 2° 5′ 30.3″ W	All study area	AHS sensor (80 bands from 0.3 to 14.8 um)
Atmospheric measurements	39° 3′ 46.4″ N 2° 5′ 33.8″ W	All study area	Aerosol optical thickness at 550 nm), water vapor and ozone

and much smaller variations in forward directions (Bacour & Breon, 2005).

Theoretically, surface albedo is defined as the ratio between the up-welling and down-welling incident irradiance upon a surface. Down-welling flux may be written as the sum of a direct component and a diffuse component. Black-sky albedo or directional–hemispherical reflectance (DHR) is defined as albedo in the absence of a diffuse component and is a function of solar zenith angle. White sky albedo or bi-hemispherical reflectance (BHR) is defined as albedo in the absence of a direct component when the diffuse component is isotropic. It is a constant. Therefore, the albedo can be written as integrals of the BRDF model through the black-sky albedo (α_{bs}) and the white-sky albedo (α_{ws}).

$$\alpha_{bs}(\theta_s, \Lambda) = \sum_k f_k(\Lambda) h_k(\theta_s) \tag{2}$$

$$\alpha_{ws}(\Lambda) = \sum_k f_k(\Lambda) H_k \tag{3}$$

where

$$h_k(\theta_s) = \int_0^{2\pi} \int_0^{\pi/2} K_k(\theta_s, \theta_v, \phi) \sin\theta_v \cos\theta_v d\theta_v d\phi \tag{4}$$

$$H_k = 2 \int_0^{\pi/2} h_k(\theta_s) \sin\theta_s \cos\theta_s d\theta_s \tag{5}$$

Since the black-sky albedo depends on the solar zenith angle, each airborne image had different black-sky albedo, but equal white sky albedo. By interpolating between black-sky and white-sky albedo quantities, the following equation can be used to compute the blue-sky (or instantaneous) albedo:

$$\alpha(\theta_s, \Lambda) = \lfloor 1 - S(\theta_s, \tau(\Lambda)) \rfloor \alpha_{bc}(\theta_s, \Lambda) + S(\theta_s, \tau(\Lambda)) \alpha_{ws}(\Lambda) \tag{6}$$

where S is the fraction of diffuse skylight that depends on the aerosol optical depth τ and on the wavelength Λ. This parameter was derived from 6S for each airborne image.

Finally, the spectral to broadband conversion was performed by following Liang (2001). Considering the spectral characteristics of AHS, we selected the MODIS equation (whose bands present the most similar response compared to AHS bands), which is written as

$$\alpha_{broadband} = 0.160\alpha_8 + 0.291\alpha_{15} + 0.243\alpha_2 + 0.116_5 + 0.112\alpha_{20} + 0.081\alpha_{35} - 0.0015 \tag{7}$$

where α_i is the blue-sky albedo of the AHS band i. Eq. (7) estimates the broadband albedo from narrowband albedo. However, these variables are often replaced by the surface bi-directional reflectance in several evapotranspiration studies (Ma et al., 2008; Ruhoff et al., 2012; Samani, Salim-Bawazi, Bleiweiss, Skaggs, & Tran, 2007, among others). This is the variation of the bi-directional reflectance during the daytime, and how it may range through different remote sensing images. In order to analyze this effect, the surface broadband albedo calculated from the BRDF was compared to the surface broadband "albedo" that was estimated by directly averaging the surface reflectance images using Eq. (7).

Finally, two broadband albedo images, derived from BRDF and surface reflectance, were estimated for each of the AHS images. These albedo images were compared in order to see the angular variations, and they were also used in the net radiation estimation.

3.3. Land surface temperature and emissivity

The long-wave component of the net radiation and most evapotranspiration algorithms need the estimation of the land surface temperature and emissivity. For this purpose, the Temperature and Emissivity Separation (TES) method proposed by Gillespie et al. (1998) was used in this work. This method was initially developed for the Advanced Spaceborne Thermal Emission and Reflection Radiometer (ASTER), although in several field campaigns even in barrax areas and using the AHS images, this method obtains satisfactory results (Sobrino, Jimenez-Munoz, et al., 2007). Once the land surface temperatures and emissivity were retrieved, the spectral emissivity (for each of the 10 thermal bands) was converted from the narrow to broadband emissivity using the simple average. Note that in this paper focus on angular effects related to the surface albedo, so angular effects on surface emissivity and/or LST will not be considered. Implications of this assumption will be discussed in Section 7.

3.4. Net Radiation estimations

The Net Radiation (Rn) was estimated using the energy balance equation:

$$Rn = (1-\alpha) RS\downarrow + \varepsilon_S RL\downarrow - RL\uparrow \tag{8}$$

where $RS\downarrow$ (W m^{-2}) is the incoming direct and diffuse shortwave radiation at surface, α is the surface broadband albedo, $RL\downarrow$ (W m^{-2}) is the incoming longwave radiation from the atmosphere, $RL\uparrow$ (W m^{-2}) is the outgoing longwave radiation emitted from the surface to the atmosphere, and ε_s is the surface emissivity.

Analyzing each variable in Eq. (9), two images of Rn were calculated by using both the broadband albedo derived from the BRDF, as well as the surface reflectance weighted average following Eq. (7). $RS\downarrow$ and $RL\downarrow$ were estimated from in-situ measurements and assumed equal for the whole the study area. In addition, $RL\uparrow$ was estimated using the equation:

$$RL\uparrow = \varepsilon_S \sigma T_S^4 \tag{9}$$

where ε_s and T_s are the surface broadband emissivity and temperature derived from AHS images, and σ is the Stefan–Boltzmann constant ($5.67 \cdot 10^{-8}$ W m^{-2} K^{-4}).

3.5. Daily evapotranspiration

Rn (W m^{-2}) can also be estimated using the following energy balance equation

$$Rn = H + LE + G \tag{10}$$

where G (W m^{-2}) is the ground flux, H (W m^{-2}) is the sensible heat flux and LE (W m^{-2}) is the latent heat flux. Thus, the variations in this magnitude, driven by the albedo variability, should affect the estimation of surface flux and, therefore, evapotranspiration. Since G, H and LE are needed to estimate the instantaneous evapotranspiration, these variables were computed using the following equations. Firstly, G flux can be derived from a proportion of Rn estimated according the surface features related to vegetation information or by including a thermal parameter such as the land surface temperature (Bastiaanssen, 2000; Su, 2002). In this work, G (W m^{-2}) flux was estimated using the method proposed by Clothier et al. (1986),

$$G = Rn\left(0.295 - 0 - 01331 \frac{\rho_{NIR}}{\rho_{IR}}\right) \tag{11}$$

where Rn (W m^{-2}) is net radiation, ρ_{NIR} and ρ_{IR} are reflectance for the red and the near infrared channels. It is important to note that a proportion of the angular effects are also included in the surface reflectance ratio. For daily evapotranspiration, G is assumed to be equal to zero.

Secondly, in order to estimate H and LE, we used the Simplified Surface Energy Balance Index (S-SEBI) method developed by Roerink et al. (2000). This method consists of a base line representative of the maximum sensible heat ($\lambda E = 0$) and the maximum potential evapotranspiration (λE = Max, $H = 0$). It is based on the evaporative fraction (EF) estimation using the surface albedo and the land surface temperature relationship. When determining EF, an approximation using Eq. (12) (according to Roerink et al., 2000; Su, Pelgrum, & Menenti, 1999; Verstraeten et al., 2005) is attempted:

$$EF_i = \frac{T_H - T_s}{T_H - T_{LE}} = \frac{a_H \alpha_0 + b_H - T_s}{(a_H - a_{LE})\alpha_0 + (b_H - b_{\lambda ET})} \quad (12)$$

where T_H is land surface temperature for dry pixels; T_{LE} is land surface temperature for wet pixels; Ts is land surface temperature; α_0 is surface albedo; a_H, a_{LE} are the slopes of the line of, respectively, the high and low temperatures as a function of surface albebo; b_H, b_{LE} are the intercepts of the line of, respectively, the high and low temperatures as a function of surface albedo. In this paper, the S-SEBI

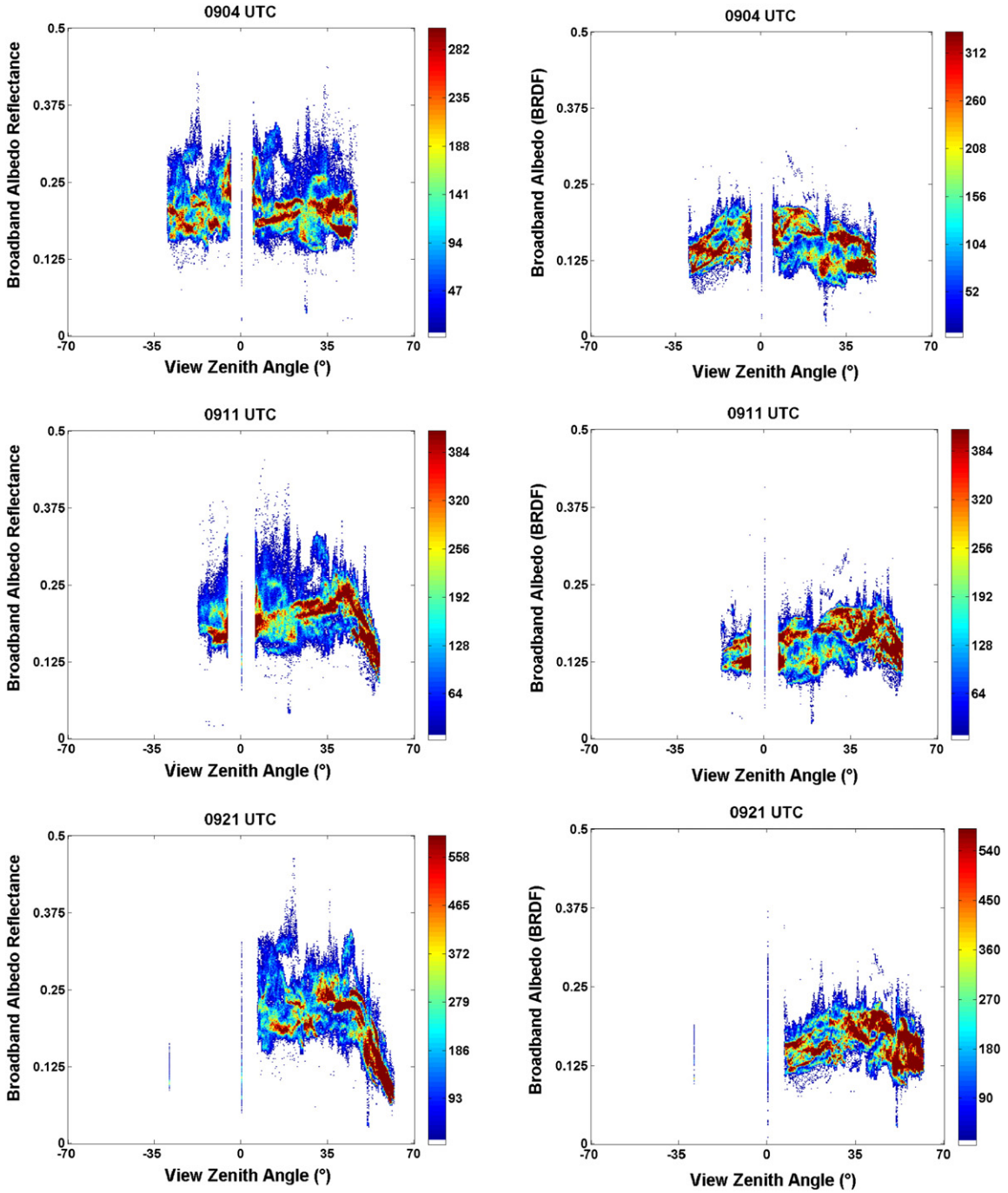

Fig. 3. Surface albedo estimated by surface reflectance (left column) and BRDF (right column) and during each overpass flight and its variation with the zenithal observations angle. The color scale legend represents the amount of pixels that belong to each ordered pair in the scatterplot.

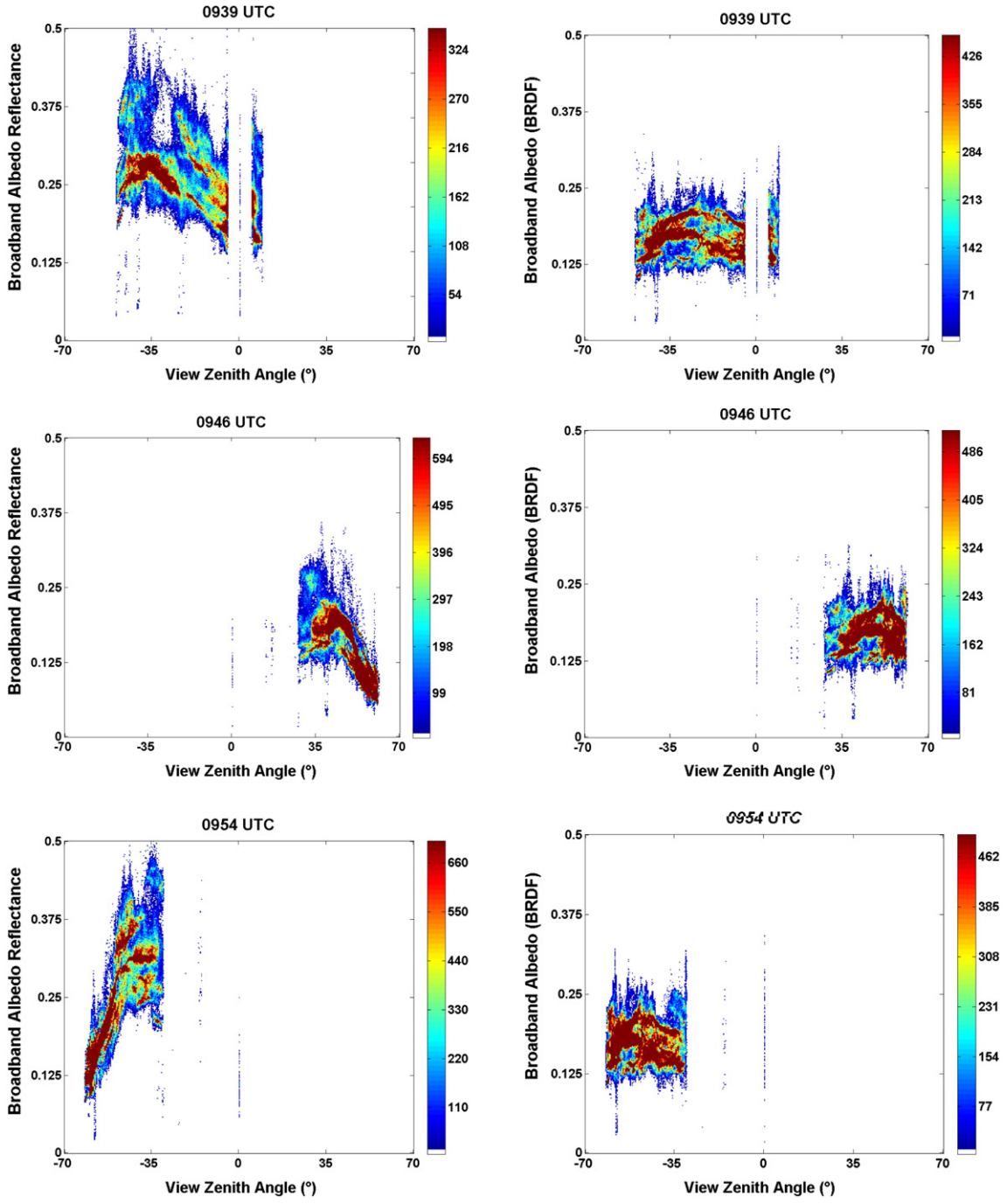

Fig. 3 (*continued*).

model was applied to estimate the surface albedos (α_{BRDF} and α_{Ref}) in order to determine the angular effects in evaporative fractions. Initially, this method was developed from Landsat imagery where the surface broadband albedo was estimated using surface reflectance (Roerink et al., 2000). Therefore, some differences can be expected when α_{BRDF} is used in the albedo/temperature diagram, and consequently the evaporative fraction is going to be influenced by this effect. Then, H (W m^{-2}) and LE (W m^{-2}) were derived from the following equations:

$$LE = EF(Rn - G) \tag{13a}$$

$$H = (1 - EF)(Rn - G) \tag{13b}$$

Finally, AHS images were used to assess the influence of angular effects on daily evapotranspiration (ET_d (mm)) using the following equations.

$$ET_d = \frac{24 \cdot 3600 \cdot EF \cdot R_{nd}}{\lambda} = \frac{24 \cdot 3600 \cdot EF \cdot C_{di} \cdot R_{ni}}{\lambda} \tag{14}$$

where R_{ni} is the net radiation for each image (instantaneous value), R_{nd} is the daily net radiation, and C_{di} is the ratio between R_{nd} and R_{ni} proposed by Seguin and Itier (1983). This value was equal to 0.315 as an average of the C_{di}. The EF at daily scale was assumed to be similar to that derived instantaneously from Eq. (12) at the time of remote sensing data acquisition (Bastiaanssen, 2000). The latent heat of vaporization was considered to be equal to 2.45 MJ/kg. For daily evapotranspiration

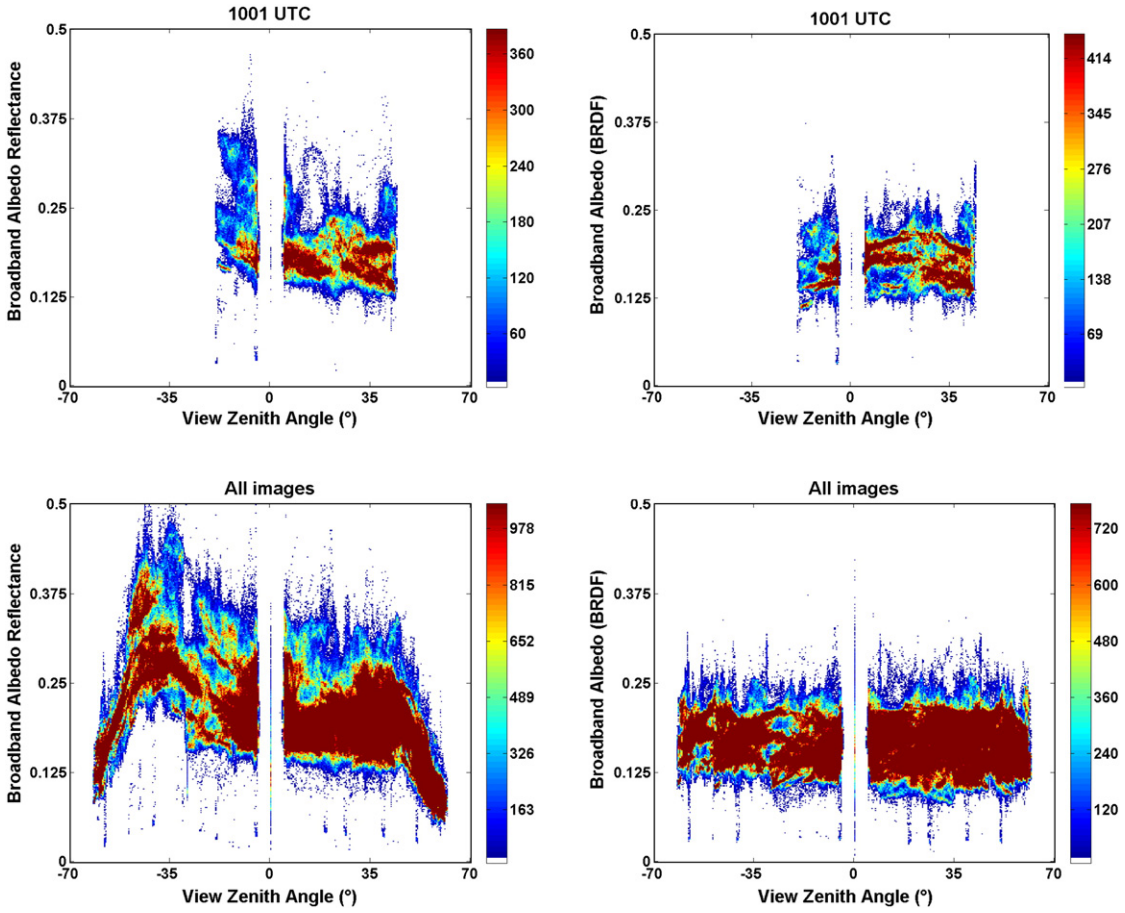

Fig. 3 (*continued*).

computation, *G*, *LE* and *H* were not considered because the term *EF* involved in Eq. (14) is computed by using Eq. (12) based on albedo and land surface temperatures, thus giving the radiative information corresponding to the maximum and minimum fluxes.

3.6. Error analysis

Assuming that all the parameters in Eq. (6) are independent (not correlated), the propagation error can be calculated in a straightforward way to estimate the impact of absolute errors on albedo and to obtain *Rn*, *G*, *H*, *LE*, *EF* and ET daily. Given a functional relationship of the shape:

$$y = f(x_1, x_2, \ldots, x_N) \tag{15}$$

The sensitivity of the dependent variables y to a generic parameter $x_1, x_2, \ldots, x_N$ can be estimated by:

$$\Delta y = \left(\frac{\partial f(x_1, x_2, \ldots, x_N)}{\partial x_1}\right)\Delta x_1 + \left(\frac{\partial f(x_1, x_2, \ldots, x_N)}{\partial x_2}\right)\Delta x_2 + \ldots + \left(\frac{\partial f(x_1, x_2, \ldots, x_N)}{\partial x_N}\right)\Delta x_N \tag{16}$$

The error propagation includes the differences between α_{REF} and α_{BRDF}. The error propagation was introduced into the model to retrieve daily evapotranspiration and *Rn*, *H*, *LE* and *EF* for three cases: one for the best scenario, one for the poorest and one medium, where the absolute errors were estimated from the albedos (α_{REF} and α_{BRDF}).

4. Intercomparison between results obtained from α_{REF} and α_{BRDF}

4.1. Albedo comparison

Fig. 3 shows the angular variability for each α_{BRDF} and α_{REF} AHS image acquired between 9 and 10 UTC. The first three images (9:04, 9:11 and 9:21) were acquired along the solar plane, while the others were acquired along the orthogonal plane. In this paper we have followed the Roujean et al. (1992) notation where negative VZA are located in the backward scattering direction and positive values are located in the forward scattering direction.

At first glance, the VZA shows strong influences on α_{REF} while not showing any on α_{BRDF}. Considering first the solar plane direction, α_{REF} decreases with an increase in VZA. Regarding the orthogonal plane, the angular effect presents the highest influence on α_{REF} at 9:54, showing similar (or slightly lower) albedo values than α_{BRDF} for high VZA (in absolute magnitude), which increases with a pronounced slope up to maximum values around 35°, which coincides with the solar zenith angle at that flight overpass time. A possible reason for this might be the hot spot effect, which consists of a peak in reflectance obtained when sun and view directions coincide with the backward scattering (Breon et al., 2002). The hot spot effect is also noticeable at 9:39 where the VZA at the center of the image was −40°. However, in this case, the surface reflectance decreases as the VZA approaches nadir. In the case of the image at 9:46 (+40°), each VZA belongs to the forward scattering direction, consequently, we do not observe any hot spot effect and there is a continuous decrease in the surface reflectance as the VZA increases. However, at 10:01 UTC, the VZA was close to Nadir and α_{REF} is least dependent on the VZA at this point. The plot including all the images shows the significant influence of VZA when its values

rise above 35°, in the case of $\alpha_{REF,}$ a clear overestimation (or underestimation) of this parameter compared to the albedo derived from BRDF integration can be clearly seen.

As an example, Fig. 4 shows the linear comparison between α_{BRDF} and α_{REF}, in addition to the spatial variability of the images at 9:39 and 10:01 UTC. As observed in Fig. 3, the highest error can be seen for the image at 9:39 UTC, which shows an RMSE of 0.11 and a clear overestimation of the albedo. The minimum differences were obtained for the VZA near the nadir (10:01 UTC), where an RMSE of 0.04 was achieved, although the albedo was slightly overestimated mainly on the borders, where the VZA showed higher values due to the high Field Of View (FOV) of the AHS sensor.

The statistics of each image are detailed in Table 2. Generally, the broadband albedo shows higher values when using the reflectance average directly, than it does at the same magnitude estimated from the BRDF integration, thus leading to negative bias. When focusing attention on the mean values, α_{BRDF} shows lower values than $\alpha_{REF,}$ and similar values when comparing each image. With reference to the bias, we get negative values in almost each case (albedo overestimation when considering α_{REF}) with the exception of the image at 9:46 UTC (+40°), which coincides with the highest VZA in the forward scattering. This may be a consequence of the shadowing effect, which reduces the surface reflectance values in this direction.

When taking all the images into account, bias is equal to −0.07 with a RMSE of 0.07. It supposes a Relative RMSE of about 39% representing a clear error source when the albedo is approximated to a weighted average of the surface reflectance. However, as analyzed in previous figures, the highest errors correspond to VZA higher than 35°. Therefore, the Lambertian assumption can be considered in case of sensors with reduced FOV and in case of near to nadir observations.

Table 2
Statistics for α_{BRDF} and α_{REF} for each AHS images following VZA and overpass time.

		α_{BRDF}	α_{REF}	$\alpha_{BRDF} - \alpha_{REF}$		
UTC hour	VZA (°)	Mean	Mean	Bias	Stddev	RMSE
9:04	40	0.15	0.21	−0.06	0.03	0.07
9:11	0	0.16	0.20	−0.04	0.03	0.05
9:21	57	0.16	0.19	−0.03	0.05	0.05
9:39	−40	0.17	0.27	−0.10	0.05	0.11
9:46	40	0.17	0.15	0.03	0.05	0.05
9:54	−57	0.17	0.24	−0.07	0.08	0.10
10:01	0	0.18	0.19	−0.015	0.03	0.04

4.2. Net Radiation

The angular effects on net radiation estimation are presented in Fig. 5. One marked feature is that the highest *Rn* belongs to water bodies. In addition, the lowest values are characterized by bare soil with sparse vegetation cover. If we compare each albedo result, the image at 9:39 shows a clear underestimation in net radiation for high VZA when the α_{REF} is used. However, there is no significant difference in *Rn* magnitude at nadir by using both α_{BRDF} or α_{REF}. In this case, α_{REF} shows a slight overestimation in vegetated fields while clearly underestimating within the case of bare soils located on the left side of the image (backward scattering direction).

Table 3 shows the statistical results for each *Rn* estimated image. Analogously to the albedo statistics, the mean value of *Rn* for each image derived using α_{BRDF} shows less standard deviation than the results for α_{REF}. Generally, using α_{REF} underestimates *Rn* showing positive bias in each flight with the exception of the image at 9:46 (+40°), which may be due to α_{REF} underestimation (shadowing effect). The highest bias and RMSE is obtained for the 9:39 and 9:54 images, which include the hot spot effect. The RMSE ranges from 30 to 85 W m^{-2}, which implies a relative error from 6 to 17%. Generally, the Lambertian assumption leads to an underestimation of 31 W m^{-2} and a RMSE of 57 W m^{-2}.

4.3. Ground heat flux

In Fig. 6, we observed lower *G* values using α_{REF} instead of α_{BRDF}, mainly in bare soils with sparse vegetation. In addition, when comparing the image at 9:39 to the one at 10:01, slightly lower values

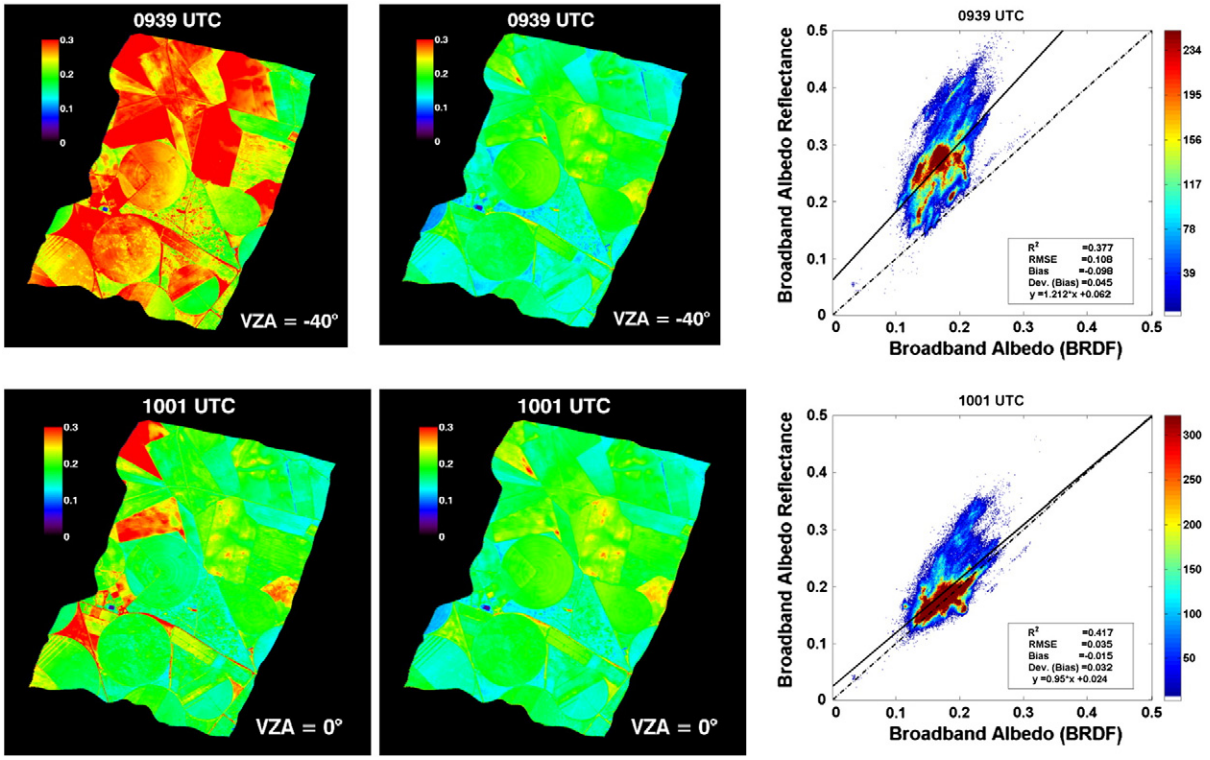

Fig. 4. Broadband surface albedo derived from reflectance and the Liang equation (left) and the BRDF integrals (Right) for each AHS overpass flight hour.

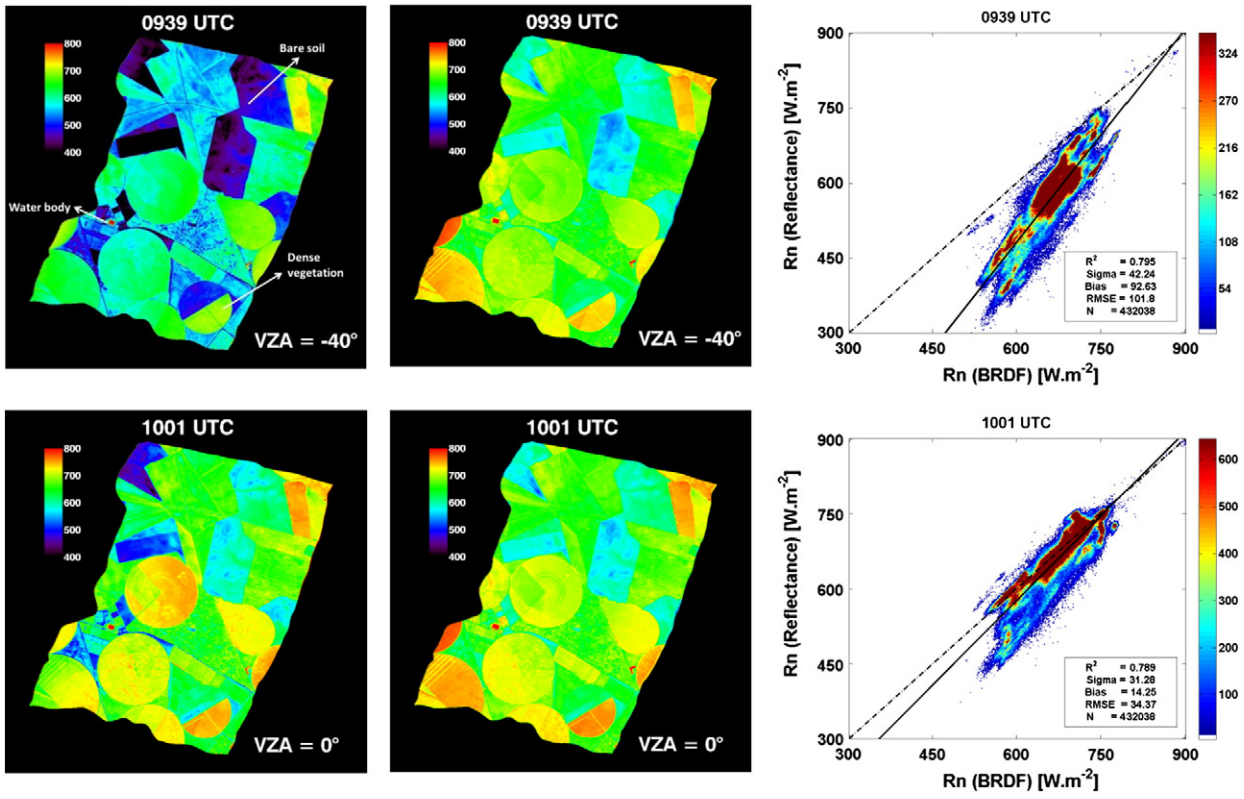

Fig. 5. Net radiation using the albedo estimated from the reflectance (left) and the BRDF (right) for each AHS overpass flight hour. Images presented for hot-spot (−40°) and Nadir VZA angles.

are obtained using either α_{REF} or α_{BRDF}. Nevertheless, no high differences were observed on *Rn* estimated from α_{REF} or using α_{BRDF}. This can be attributed to the equation used for estimating *G*, because Eq. (3) (derived by Clothier et al. (1986)) considers *G* to be equal to the net radiation multiplied by a term that includes the ratio between the Near Infrared and the Red surface reflectance. Differences between G estimations and G measured in-situ (Fig. 6) could be explained by the low sensitivity of the NIR/IR ratio to capture local variations of litter, soil moisture and soil texture. In a first approximation, the ratio between the reflectances should minimize the angular effects. However, rationing of the NIR and red spectral bands does not remove surface anisotropy due to the spectral dependence of the BRDF response (Gutman, 1991; Roujean et al., 1992). Therefore, when multiplying this term by *Rn*, this ratio angular dependency may minimize *Rn* estimations. Nevertheless, at daily level G can be assumed close to zero (Gomez, Olioso, Sobrino, & Jacob, 2005; Seguin & Itier, 1983), so errors on G estimation do not affect to estimations of daily ET.

Table 3
Statistics of *Rn* for each AHS images following VZA and overpass time.

UTC hour	VZA (°)	α_{BRDF} Mean (W m^{-2})	α_{REF} Mean (W m^{-2})	$\alpha_{BRDF} - \alpha_{REF}$ Bias (W m^{-2})	Stddev (W m^{-2})	RMSE (W m^{-2})
9:04	40	460	418	43	24	49
9:11	0	487	457	30	24	39
9:21	57	505	485	21	35	41
9:39	−40	490	413	77	35	85
9:46	40	536	557	−20	37	42
9:54	−57	540	484	56	65	85
10:01	0	524	511	12	27	30
Total				31	48	57

4.4. S-SEBI diagram

In the S-SEBI algorithm, the evaporative fraction is obtained from the Surface Temperature and Albedo diagram. Fig. 7 shows the scatter-dispersion between α_{REF} and α_{BRDF} against LST. Analogously to the previous figures, we present the plots for only two images, 9:39 UTC (−40° VZA) and 10:01 UTC (0° VZA). Each image include some pixels of water bodies with minimum values of LST and minimum albedo values located at the bottom of the wet boundary. 9:39 UTC shows high variability of the α_{REF} albedo ranging between 0.15 and 0.45. In addition, we observe a lower range of α_{REF} values, fluctuating from 0.15 to 0.35 during the nadir pass at 10:01, showing a high pixel frequency around 0.2. However, despite the 9:39 UTC image's high variability, H_{max} presents similar fitting values and the LET_{max} linear fitting parameters are slightly modified. Centering attention on the LST-α_{BRDF} diagrams, the albedo shows less variability than α_{REF}, ranging from 0.1 to 0.25 in both images. This low albedo variation is due to the low heterogeneity of land cover types along the main area during this time period. Furthermore, H_{max} presents a slightly different slope when comparing the 9:39 to 10:01 UTC images when using α_{BRDF}, while its intercept as well as LE_{max} linear fit parameters show similar results.

Table 4 shows the linear fit parameters of all the LST-albedo diagrams and the mean and standard deviation of each parameter. Comparing α_{REF} to α_{BRDF} results, we obtain similar average of H_{max} parameters, while LE_{max} shows different values. In fact, α_{REF} leads to significantly higher slopes than α_{BRDF}. The table shows similar standard deviation for each parameter, although in the case of α_{LE} when using α_{BRDF} corresponds to a much lower average than α_{REF}. When we compare each flight, *H* presents the highest difference at 9:54 UTC, when

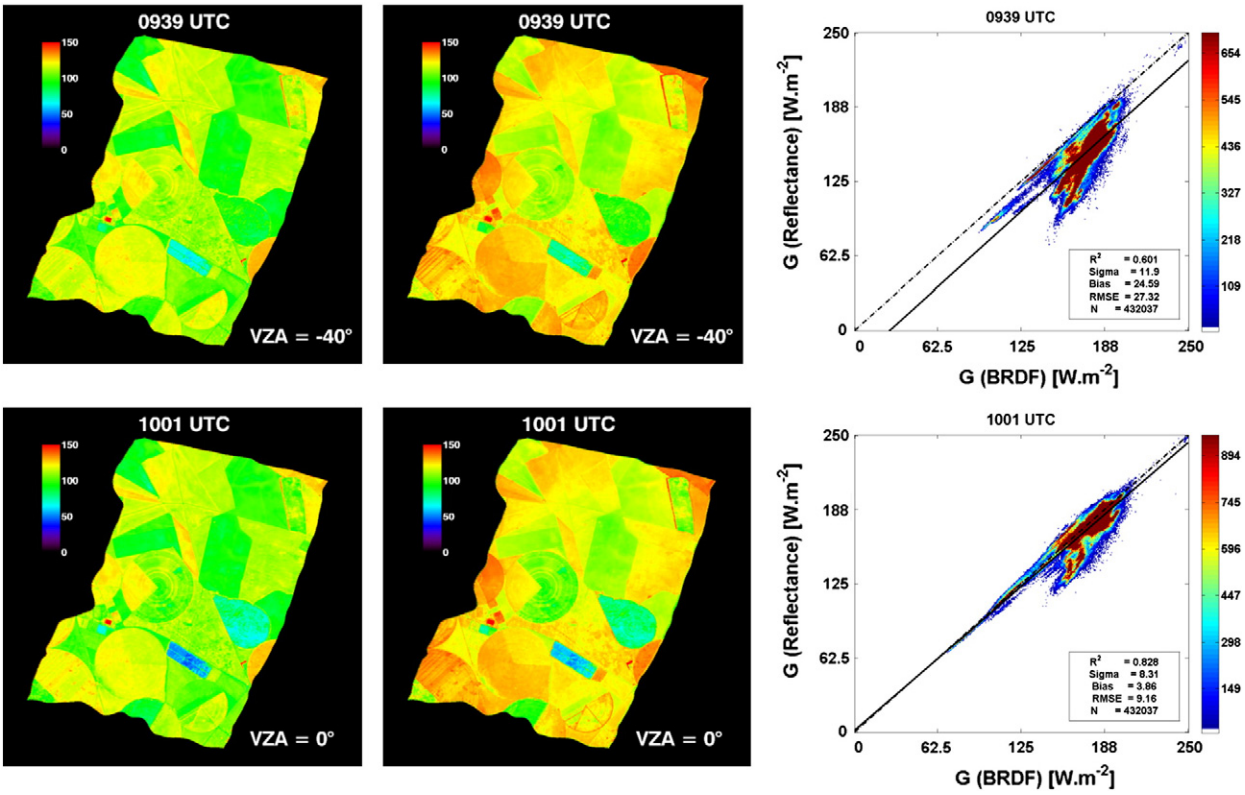

Fig. 6. G estimations using the albedo estimated from the reflectance (left) and the BRDF (right) 9:39 and 10:01 images (hot-spot (−40°) and Nadir VZA angles).

nominal VZA was −57° in the orthogonal plane and *LE* shows the maximum difference at 9:04 and at 9:21 UTC whose corresponding VZA were 40° and 57° in the solar plane respectively.

The results from the table analysis regarding *H* parameters show similar results (on average), independently of the approximation considered. H_{max} linear fit represents areas with low soil moisture content, such as bare soil, fallow land and barren areas where the increase in surface albedo leads to a decrease in surface temperature. In contrast, LE_{max} corresponds to areas where the increase in albedo leads to increase in temperature. These areas represent irrigated fields where all the energy provided by the increase in temperature is employed in the evaporation process. Results show that they had the most significant changes when considering α_{REF} instead of α_{BRDF}.

4.5. Evaporative fraction (EF)

In order to evidence the angular influences on the *EF*, Fig. 8 shows the *EF* estimated at 40° and nadir. Basically, no strong differences are observed between the *EF* calculated using α_{BRDF} and α_{REF}. In fact, as seen in Table 4, these images do not represent significant differences between H_{max} and LE_{max} parameters. We observe a slight increase in *EF* in barren areas when comparing 9:39 to 10:01 UTC images both from α_{BRDF} and α_{REF}. Additionally, *EF* shows slightly lower values in vegetated areas at 10:01 UTC using α_{REF} or α_{BRDF}.

4.6. H, LE and daily evapotranspiration

Fig. 9 shows *H* estimation for observation angles close to nadir and at −40°. We observe a slight underestimation when α_{REF} is used for the 9:39 UTC image. However, this underestimation is more evident in the cover types with sparse vegetation. This effect is also observed in the case of the near nadir image but there is less difference than using α_{REF}. When comparing the 9:39 image to the 10:01 UTC image, *H* showed stable values when using α_{BRDF}. However, in the case of α_{REF}, the near to nadir image presents slightly lower *H* values for bare soils and slightly higher values for vegetated fields than for 10:01 UTC image.

In the case of *LE* images (Fig. 10), crops with denser vegetation present higher values of latent heat when using α_{BRDF} both at 9:39 and at 10:01 UTC. This suggests that using α_{REF} to obtain *LE* may underestimate the latent flux over dense crops. In barren areas, α_{REF} leads to slightly higher values than α_{BRDF}, although this is more obvious at 9:39 UTC. *LE* shows stable values using both α_{BRDF} and α_{REF}.

Finally, Fig. 11 shows daily ET images. The α_{REF} leads to ET underestimation in the case of vegetated areas and overestimation in barren areas when compared to α_{BRDF} at 9:39 UTC, while presenting similar values at 10:01 UTC (near nadir image). Comparing the 9:39 and 10:01 UTC images, we obtained stable values when using α_{BRDF}, while α_{REF} shows values that are higher and more similar to α_{BRDF} at 10:01 UTC. These results show that remotely sensed data acquired with VZA higher than 35°–40° can lead to wrong ET values when the Lambertian assumption is used to derive the surface albedo.

Tables 5, 6 and 7 summarize the statistical results for *H*, *LE* and daily ET estimations for all available image acquisitions. For *H*, α_{REF} underestimates this value on each flight, obtaining an overall bias of 29 W m^{-2} with respect to α_{BRDF}. Additionally, the mean value for each flight shows a higher amplitude than when using α_{BRDF}. The greatest difference between using α_{REF} instead of α_{BRDF} corresponds to the 9:21 UTC image (57° in the solar plane), which leads to an error of 53 W m^{-2}. The RMSE for each image ranges between 29 and 53 W m^{-2}, which implies a relative error from 23% to 39%. The total RMSE when using all images is 38 W m^{-2}. This value supposes a relative error of 30%.

For the case of *LE*, these results show less difference between α_{REF} and α_{BRDF} with RMSE from 13 to 37 W m^{-2} (relative errors between 6 and 18%). We obtained a total bias of 2 W m^{-2} and a RMSE of 24 W m^{-2}, which implies a relative error of 12%. Finally, no significant differences are observed in daily ET average values through the images with the exception of the flights at 9:21 and 9:46 UTC (57° in the solar plane and 40° in the orthogonal plane respectively), where α_{REF}

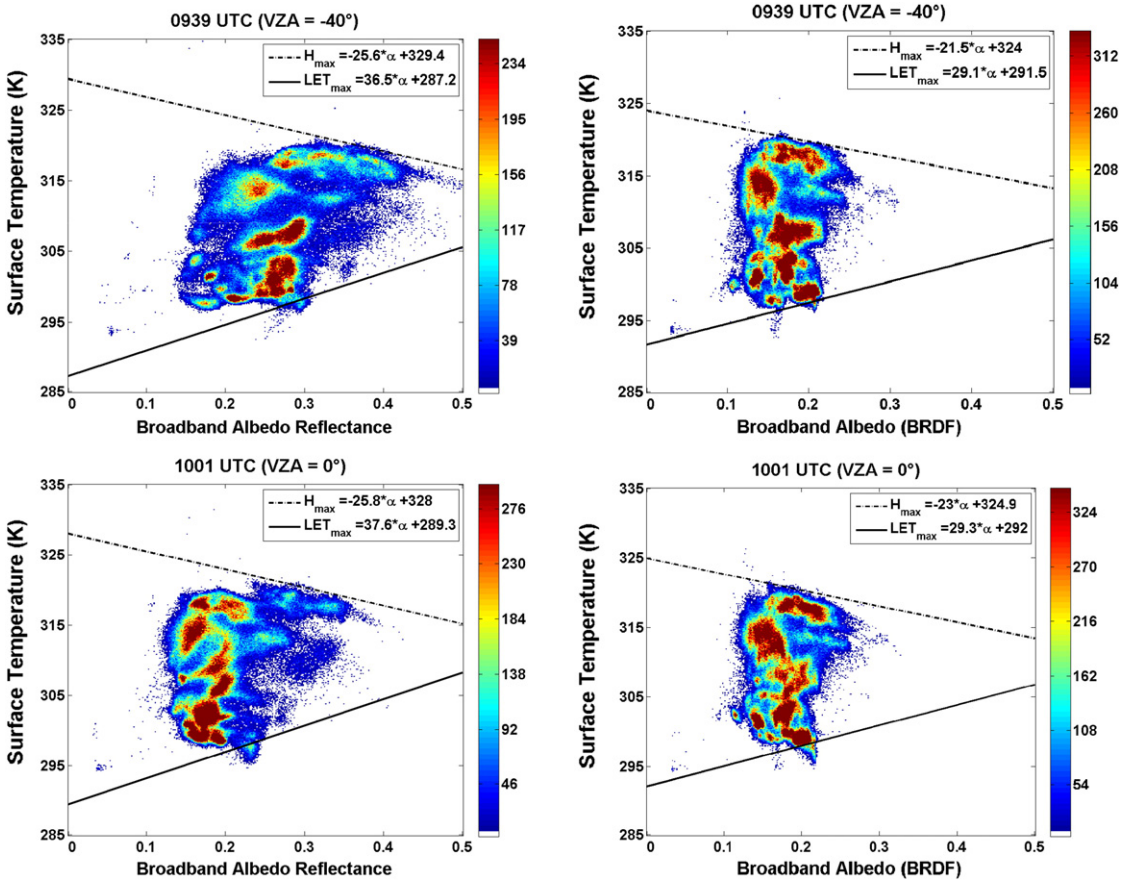

Fig. 7. Albedo–surface temperature relationship for the S-SEBI model for 09:39 UTC and 1001 UTC, representing the hot-spot and the Nadir VZA. Plots are alos indicating the upper and lower boundaries according to wet and dry surface assumptions. Each baseline was obtained using 5000 classes. Left column uses the albedo derived from reflectance and right column the albedo by using the BRDF.

overestimates the average *ET*. The total RMSE for each image shows values ranging from 0.23 to 0.66 mm day^{-1} which means a relative error from 5% to 15%. Generally, when taking all the flights into consideration, daily ET images present a general bias of −0.10 mm day^{-1} (higher ET values using α_{REF} instead of α_{BRDF}), a standard deviation of 0.38 mm day^{-1} and an RMSE of 0.4 mm day^{-1}.

5. Comparison with in-situ data

5.1. Wheat meteorological tower

Fig. 12 shows the comparison of *Rn*, albedo and ground flux on the wheat field where the meteorological station was placed. We did not evaluate *LE*, *H* and *EF* in this pixel since the flux tower did not have a Bowen station.

The surface broadband albedo shows good results both in the solar and in the orthogonal plane with an RMSE of 0.01 when considering α_{BRDF}, and 0.03 when using α_{REF}. The main source of error in the case of α_{REF} occurs when the VZA is equal to 35° in the orthogonal plane and the backscattering direction, which coincides with the hot spot effect. We do not observe significant differences between α_{REF} and α_{BRDF} regarding the other VZA.

In the case of net radiation, in-situ measurements present similar magnitudes to airborne Net *Rn* when using α_{BRDF}, leading to an RMSE of 12 W m^{-2}. Moreover, *Rn* using α_{BRDF} do not present any angular dependency. In the case of *Rn* from α_{REF}, a high underestimation is observed for VZA equal to 35° in the orthogonal plane and the backscattering direction, which generates the maximum bias of about 60 W m^{-2} (Rn(in-situ) − $Rn(\alpha_{REF})$). This must be a consequence of the albedo overestimation in this VZA due to the hot spot. In the case of α_{REF}, the RMSE is 27 W m^{-2}.

Finally, the soil heat flux evaluation does not present any noticeable difference when α_{BRDF} or α_{REF} was used to compute this flux magnitude. Both *G* estimations present similar RMSE (around 41 and 40 W m^{-2} for α_{BRDF} and α_{REF} respectively) with a high bias (−40 and −39 W m^{-2} respectively) along the solar and orthogonal plane. The airborne data overestimation may have two different error sources: the Clothier et al. (1986) algorithm and the accuracy of in-situ measurements. First, this algorithm has been analyzed in previous works, such as Payero, Neale, and Wright (2005) where they obtained an RMSE of 37.4 W m^{-2} in a wheat field, which is very similar to our results. Secondly, the instrument used to measure *G* was the HFP01SC heat flux plate whose nominal accuracy is ±3 W m^{-2}. However, Sauer, Meeka, Ochsnerb, Harrisc, and Hortond (2003) evaluated six

Table 4
Linear fit parameters of every LST-albedo diagram, mean and standard deviation.

UTC hour	VZA (°) center	a_H (K)		b_H (K)		a_{LE} (K)		b_{LE} (K)	
		α_{REF}	α_{BRDF}	α_{REF}	α_{BRDF}	α_{REF}	α_{BRDF}	α_{REF}	α_{BRDF}
9:04	40	−51.8	−38.9	328	321	37.9	2.0	286	294
9:11	0	−42.9	−25.3	327	320	31.2	19.9	288	291
9:21	57	−39.7	−42.0	328	324	64.1	15.3	282	290
9:39	−40	−25.6	−21.5	329	324	36.5	29.1	287	292
9:46	40	−15.0	−36.1	321	325	43.3	18.8	287	290
9:54	−57	−9.1	−56.0	324	332	52.5	52.2	281	282
10:01	0	−25.8	−23.0	328	325	37.6	29.3	289	292
Mean		−30.0	−34.7	326	324	43.3	23.8	286	290
Stddev		15.5	12.4	3.0	4.0	11.3	15.6	3.0	4.0

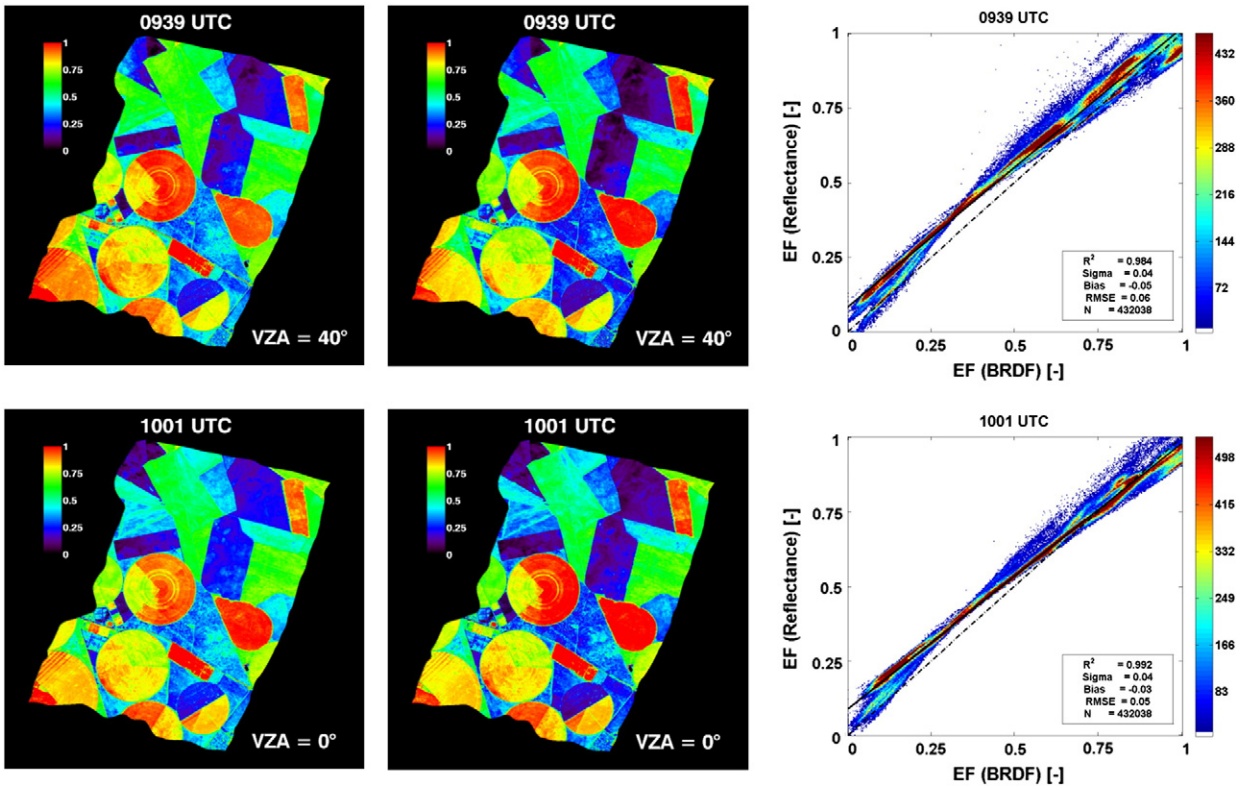

Fig. 8. *EF* using the albedo from the REF (left) and BRDF (right) at Nadir (VZA = 0°) and VZA = 40°.

types of commercially available heat flux plates with varying thickness, surface area, and thermal conductivity. Their results showed that the flux plates underestimate *G* in the dry sand by 2.4 to 38.5%. In order to improve soil heat flux plate measurements, they need to be corrected for heat stored above the soil heat flux plates, although for this study such measurements were not available.

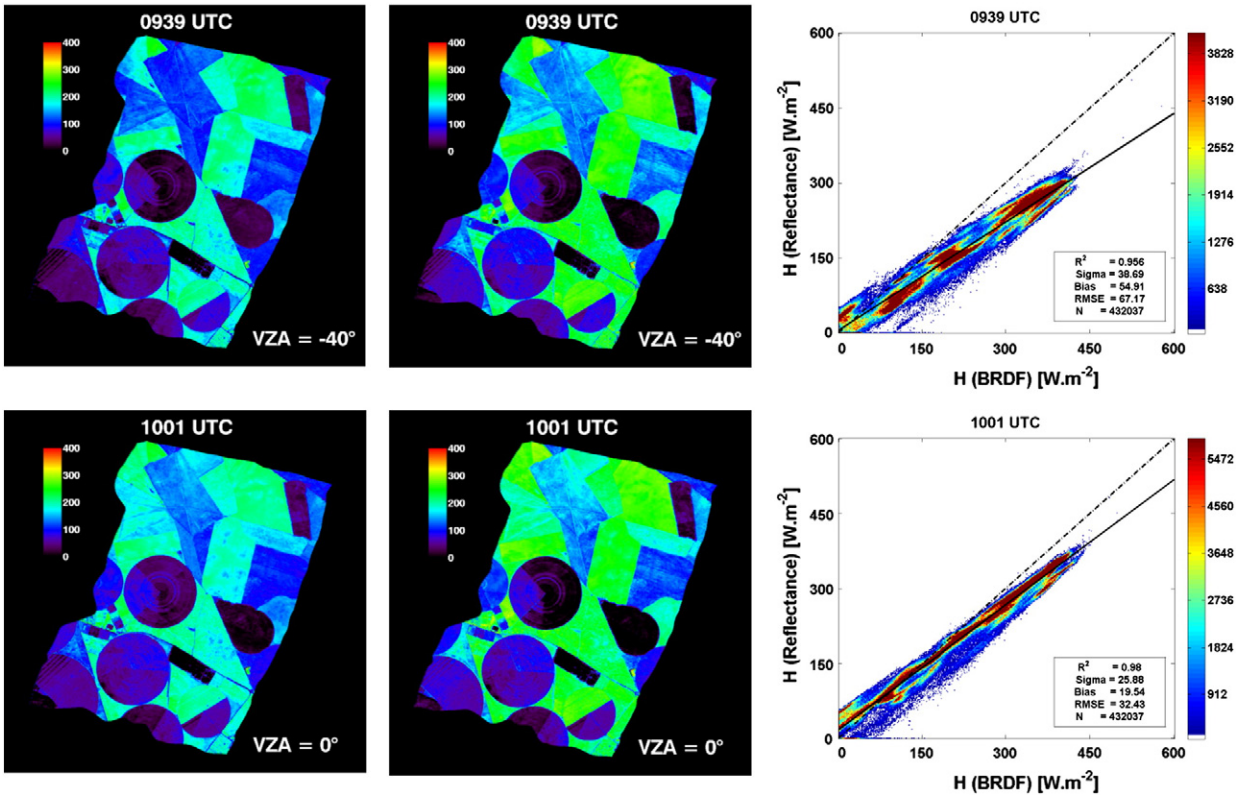

Fig. 9. *H* (W/m^2) from α_{REF} (left) and from α_{BRDF} (right) at near to nadir VZA and VZA = −40°.

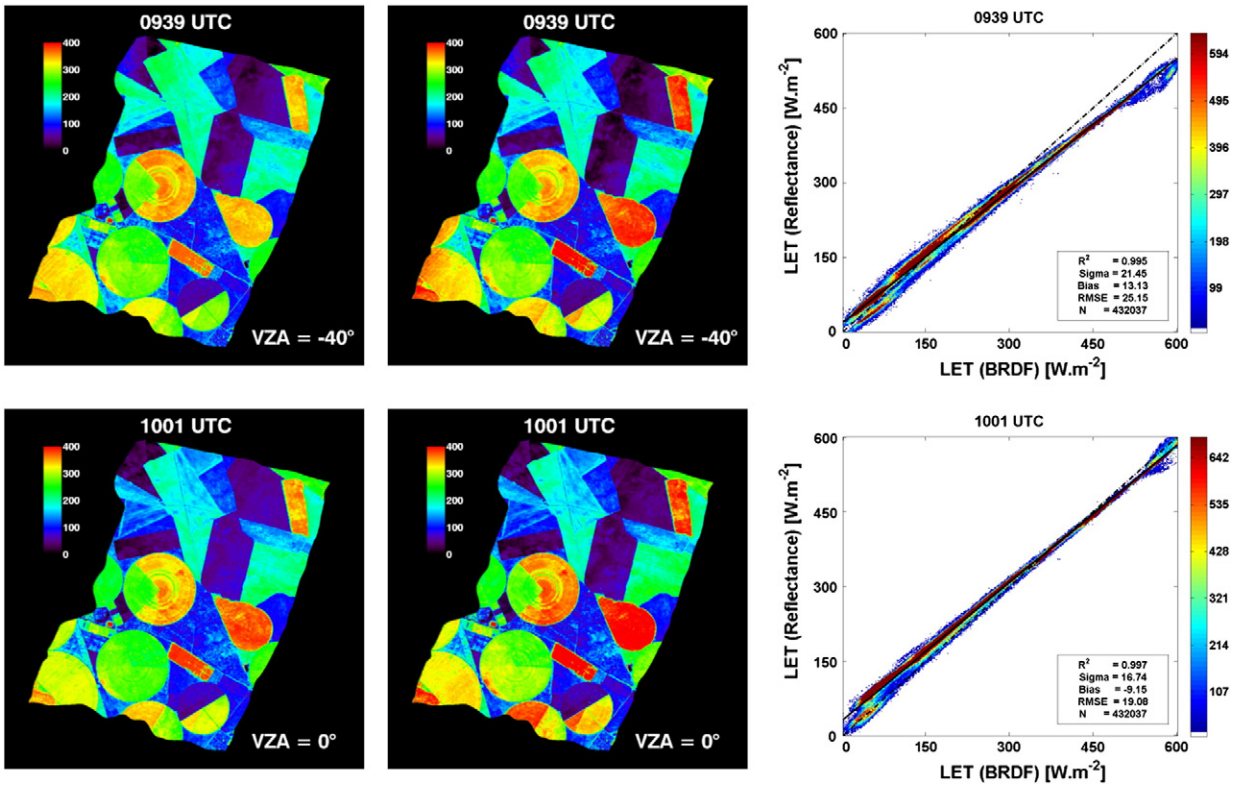

Fig. 10. *LE* (W/m^2) from α_{REF} (left) and from α_{BRDF} (right) at near to nadir VZA and VZA = −40°.

5.2. Barley eddy covariance tower

Fig. 13 presents the comparison for albedo and *Rn* on the barley field where the eddy covariance and meteorological station were placed. Comparing α_{BRDF} to in-situ measurements, the surface broadband albedo shows good results in the orthogonal plane while showing a constant bias of 0.04 and an airborne underestimation in the solar plane. α_{REF} shows a high angular variability both in the solar and orthogonal

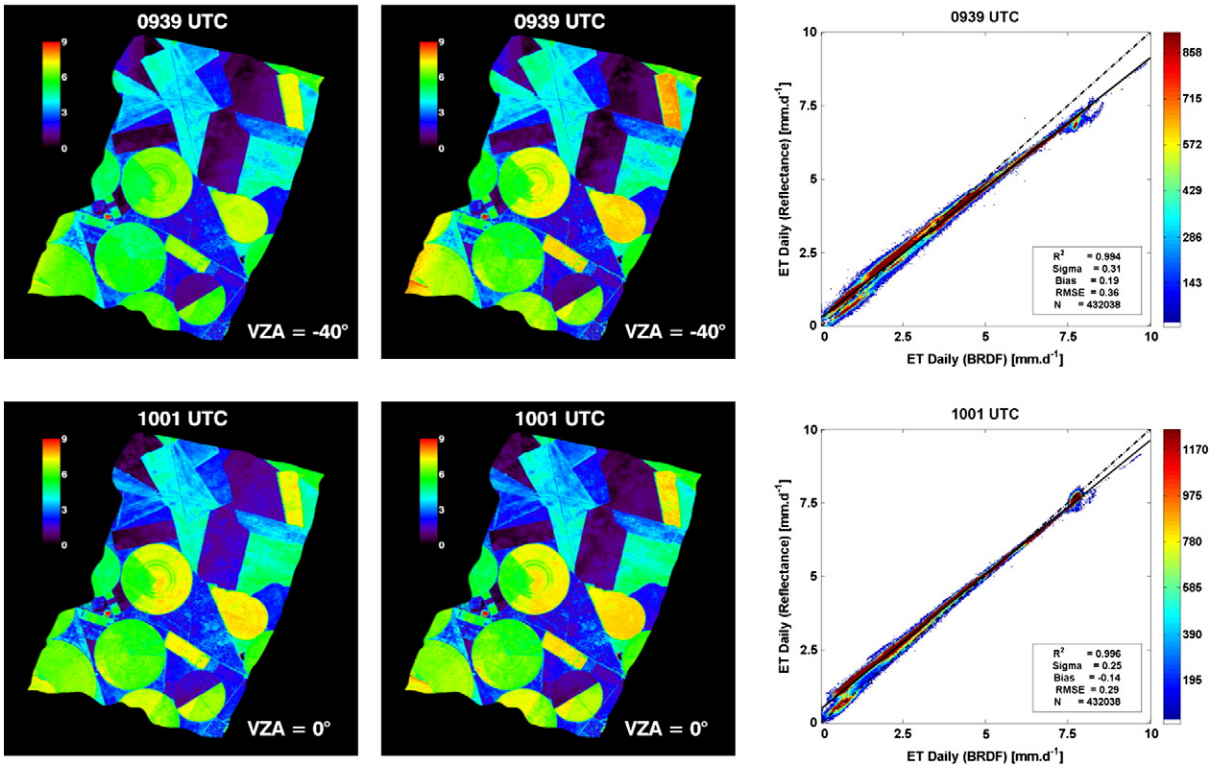

Fig. 11. Daily ET (mm) images from α_{REF} (left) and α_{BRDF} (right) at Nadir (VZA = 0°) and VZA = −40°.

Table 5
Statistics of *H* for each AHS image following VZA and overpass time.

		$H(\alpha_{BRDF})$	$H(\alpha_{REF})$	$H(\alpha_{BRDF})$–$H(\alpha_{REF})$		
UTC hour	VZA (°)	Mean (W m^{-2})	Mean (W m^{-2})	Bias (W m^{-2})	Stddev (W m^{-2})	RMSE (W m^{-2})
9:04	40	143	117	26	20	33
9:11	0	141	111	30	17	34
9:21	57	136	93	42	32	53
9:39	−40	150	118	31	22	38
9:46	40	127	106	21	20	29
9:54	−57	135	106	29	29	40
10:01	0	150	125	25	25	36
Total				29	25	38

Table 7
Statistics of daily *ET* for each AHS image following VZA and overpass time.

		$ET_d(\alpha_{BRDF})$	$ET_d(\alpha_{REF})$	$ET_d(\alpha_{BRDF})$ − $ET_d(\alpha_{REF})$		
UTC hour	VZA (°)	Mean (mm)	Mean (mm)	Bias (mm)	Stddev (mm)	RMSE (mm)
9:04	40	4.28	4.18	0.10	0.36	0.37
9:11	0	4.38	4.47	−0.09	0.25	0.27
9:21	57	4.51	5.04	−0.53	0.39	0.66
9:39	−40	3.94	3.69	0.25	0.32	0.41
9:46	40	4.68	5.03	−0.36	0.24	0.43
9:54	−57	4.47	4.46	0.01	0.23	0.23
10:01	0	3.87	3.99	−0.12	0.23	0.26
Total				−0.10	0.38	0.40

plane. It is highly overestimated in the backscattering direction while being similar to in-situ measurements in the forward scattering direction and VZA lower than 40° in the solar plane. The total RMSE is 0.03 when considering α_{BRDF} and 0.05 when using α_{REF}.

In the case of net radiation, in-situ measurements present similar magnitudes to airborne *Rn* when using α_{BRDF} in the orthogonal plane, while airborne measurements overestimate the *Rn* by around 20 W m^{-2} in the solar plane. In the case of *Rn* from α_{REF}, an angular variability is observed leading to a high underestimation in the orthogonal plane. In the case of the solar plane, *Rn* is underestimated for VZA lower than 40° while it is overestimated in the case of 50° VZA. The total RMSE is 24 W m^{-2} for α_{BRDF} and 58 W m^{-2} for α_{REF}.

Net radiation and albedo can be directly compared to pixel values from AHS images, while for turbulent fluxes comparison (*LE* and *H*), footprint theory should be used. In fact, the footprint of a turbulent flux measurement defines the source areas of the measured vertical fluxes, which can be estimated with different footprint models (Hsieh, Katul, & Chi, 2000; Kljun et al., 2004; Schmid, 1994). In this study, a two-dimensional footprint model is used (Detto, Montaldo, Alberston, Mancini, & Katul, 2006) based on the original one-dimensional model of Hsieh et al., 2000. It is defined as:

$$f(x,y,z_m) = \frac{1}{k^2x^2\sqrt{2\pi\sigma_y}} Dz_u^P |L|^{1-P} e^{\left(\frac{-Dz_u^P|L|^{1-P}}{k^2x}\right)} e^{-0.5\left(\frac{y}{\sigma_y}\right)^2} \quad (17)$$

where *L* is the Obukhov length, *D* and *P* are similarity constants for unstable, neutral and stable atmospheric conditions, *x* is the footprint in the upwind direction, *k* is von Karman's constant, σ_y is the standard deviation of the cross wind direction and z_u is a length scale expressed as

$$Z_u = Z_m\left(\ln\left(\frac{Z_m}{Z_0}\right) - 1 + \frac{Z_0}{Z_m}\right) \quad (18)$$

Table 6
Statistics of *LE* for each AHS image following VZA and overpass time.

		$LE(\alpha_{BRDF})$	$LE(\alpha_{REF})$	$LE(\alpha_{BRDF})$–$LE(\alpha_{REF})$		
UTC hour	VZA (°)	Mean (W m^{-2})	Mean (W m^{-2})	Bias (W m^{-2})	Stddev (W m^{-2})	RMSE (W m^{-2})
9:04	40	199	194	5	17	17
9:11	0	201	200	2	13	13
9:21	57	206	217	−11	36	37
9:39	−40	191	191	0	15	15
9:46	40	215	204	11	23	25
9:54	−57	205	202	3	29	29
10:01	0	192	186	6	16	17
Total				2	23	24

So *H*, *LE* and ET maps from AHS images are integrated as a weighted sum over the station source area in order to be comparable to ground data.

$$\overline{F} = \frac{\sum_{i=1}^{n} f(x_i,y_i,z_m)F(x_i,y_i)}{\sum_{i=1}^{n} f(x_i,y_i,z_m)} \quad (19)$$

where *i* is the position of a pixel in an image, *F* is the flux value in each pixel and $\overline{F}$ is the average flux in the footprint area. Regarding turbulent fluxes comparison, Fig. 14 shows *H*, *LE* and daily ET in comparison to in-situ data.

Sensible heat fluxes computed using both α_{REF} and α_{BRDF} are clearly underestimated with respect to ground data in the solar plane at 20° in the orthogonal plane. Backward scattering at 50° in the orthogonal plane images lead to good results when using α_{BRDF}. Nevertheless, ground data should be considered with caution as one can notice the sudden increase of *H* by almost 100 W m^{-2} at 10:01, which is closely linked to atmospheric turbulence. Finally, taking into account all acquisitions, *H* presents an RMSE of 88.7 W m^{-2} when using α_{REF} and 79.6 W m^{-2} when considering α_{BRDF}.

For latent heat flux, both estimations from AHS images are in good agreement with in-situ measurements with an RMSE of 40 for α_{REF} and 49.1 W m^{-2} for α_{BRDF}. *LE* in the solar plane for VZA lower than 40° is clearly overestimated, which is probably related to the way that the S-SEBI model estimates the *EF* and therefore the *LE*.

6. Error analysis

The results of the error propagation analysis are shown in Table 8. In all these cases, the albedo ranged between 21.4%, 43.3% and 65.4%. These variations affect the relative error on net radiation about 4.9%, 9.9% and 14.8% respectively. The ground flux varied in the same proportion than the *Rn*, since it was estimated using this parameter. In case of the evaporative fraction, the relative errors between 8.8 and 22% were obtained at low and high variations respectively. The relative error in daily ET for the best, poorest and medium cases were 13%, 37% and 25% respectively. Clearly instantaneous and daily ET is highly dependent on error propagation, which should therefore be kept in mind when trying to improve the accuracy of ET estvon Karman's constant, σ_y is the standard deviation of the cross wind direction andimation.

7. Discussion

Surface broadband albedo is crucial for obtaining reliable estimations related to land surface fluxes, specifically when different methods are used with the available information. Results demonstrate that surface broadband albedo derived from BRDF integration has better performance than surface reflectance does. This latter approximation is widely

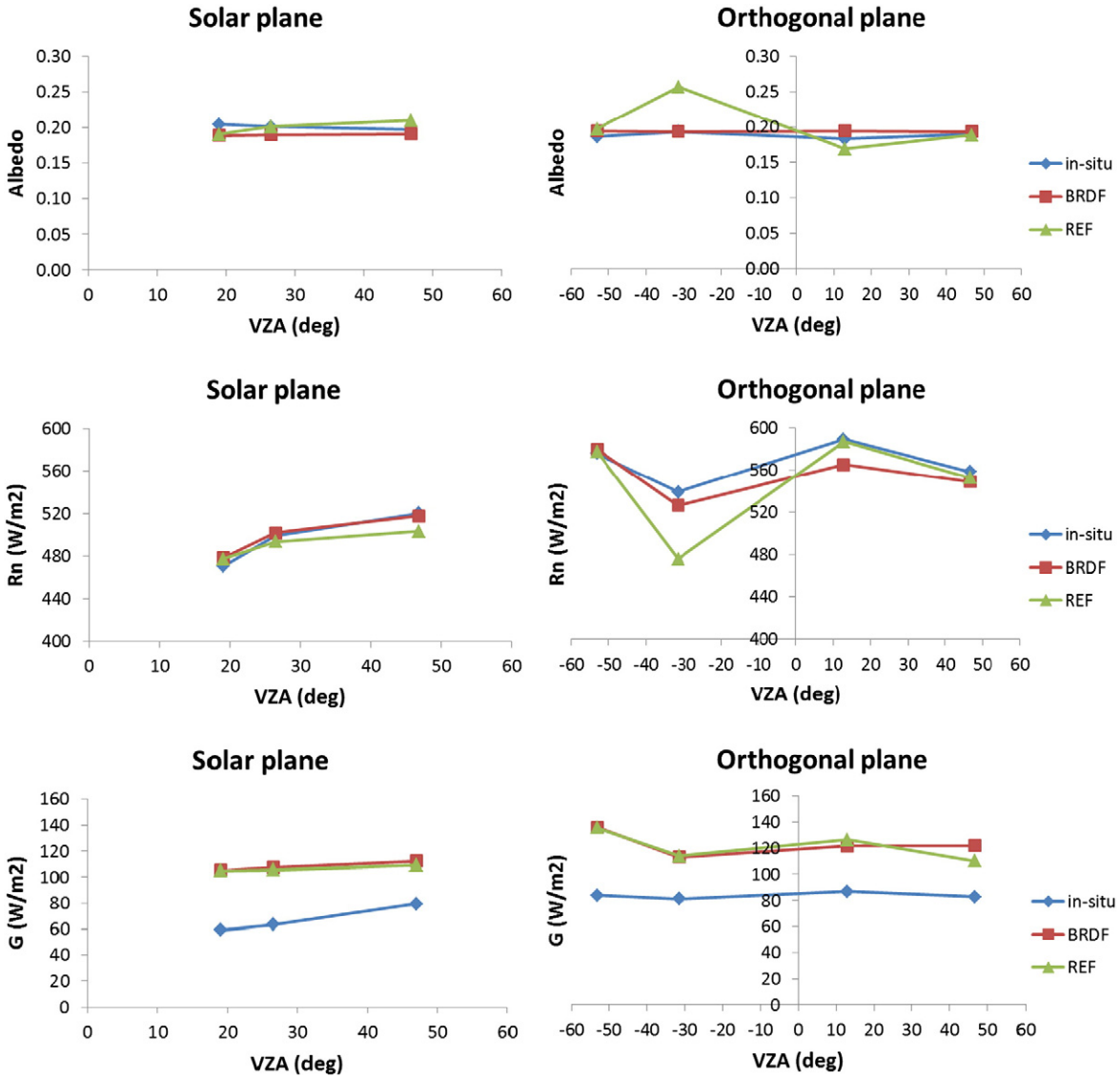

Fig. 12. Wheat field surface broadband albedo, net radiation (W m^{-2}) and soil heat flux (W m^{-2}) time series comparison for each VZA differing between solar and orthogonal planes.

used in research without any constraint on its influence on land surface flux results.

The S-SEBI method was developed using a single area of a Landsat scene, so that non broadband albedo using the surface albedo from BRDF integration could be tested beforehand. The influences on S-SEBI, mainly on the evaporative regime, are highly relevant whenever α_{BRDF} or α_{REF} are used. However, in the radiative regime, the influences of α_{BRDF} or α_{REF} were not easy to demonstrate.

Using error propagation analysis, the influence of α_{BRDF} or α_{REF} on daily evapotranspiration ranges between 13 and 37%. These results represent a relative error in the surface broadband albedo of between 21% and 60%. In fluxes (*Rn*, *H* and *LE*), the error ranges between 9% and 20%. Therefore, angular influences on surface flux, mainly in evapotranspiration, have to be taken into account for accurate results. These results lead to an error in daily evapotranspiration of about 1 or 2 mm d^{-1}. Similar results were presented in Gomez et al. (2005), who retrieved similar impact on daily evapotranspiration using airborne images. Other similar results were evidenced in Verstraeten et al. (2005), where the variation in daily evapotranspiration was estimated using satellite images at coarse spatial resolution.

Despite the fact that surface albedo can affect net radiation and therefore daily evapotranspiration, the results can be smoothed by using S-SEBI. This method was shown to be a simpler method, one that is not problematic in terms of evapotranspiration retrieval accuracy (Sobrino, Gómez, et al., 2005). In fact, computations from SEBAL or similar models need to determine roughness length, which is a difficult task, and no classical remote sensing method has been proven to be accurate enough for retrieving this variable well (Gomez et al., 2005).

S-SEBI uses the relative diagram temperature–albedo to estimate the radiative and evaporative regimes. This approach can be considered a potential strength of this method, which can be used in different cover terrains and at different spatial scales. However, the relative basis of S-SEBI may neglect the real influences of albedo estimation over *LE* and *H*, instead of the influences of albedo over the *Rn*, which may be directly related to albedo. It seems that more analysis is needed in order to analyze in detail the real potential and drawbacks of the S-SEBI method.

Remote sensing based ET models are currently most suited for the estimation of ET at both field and regional (basin) scales (Gowda, Chavez, Colaizzi, Evett, Howell, & Tolk, 2008). While field scale ET measurements are mostly produced from high to medium resolution satellite data (e.g. ASTER or Landsat), regional (basin) scale measurements are produced from coarse resolution satellite data such as MODIS (Velpuri, Senay, Singh, Bohms, & Verdin, 2013). ET products

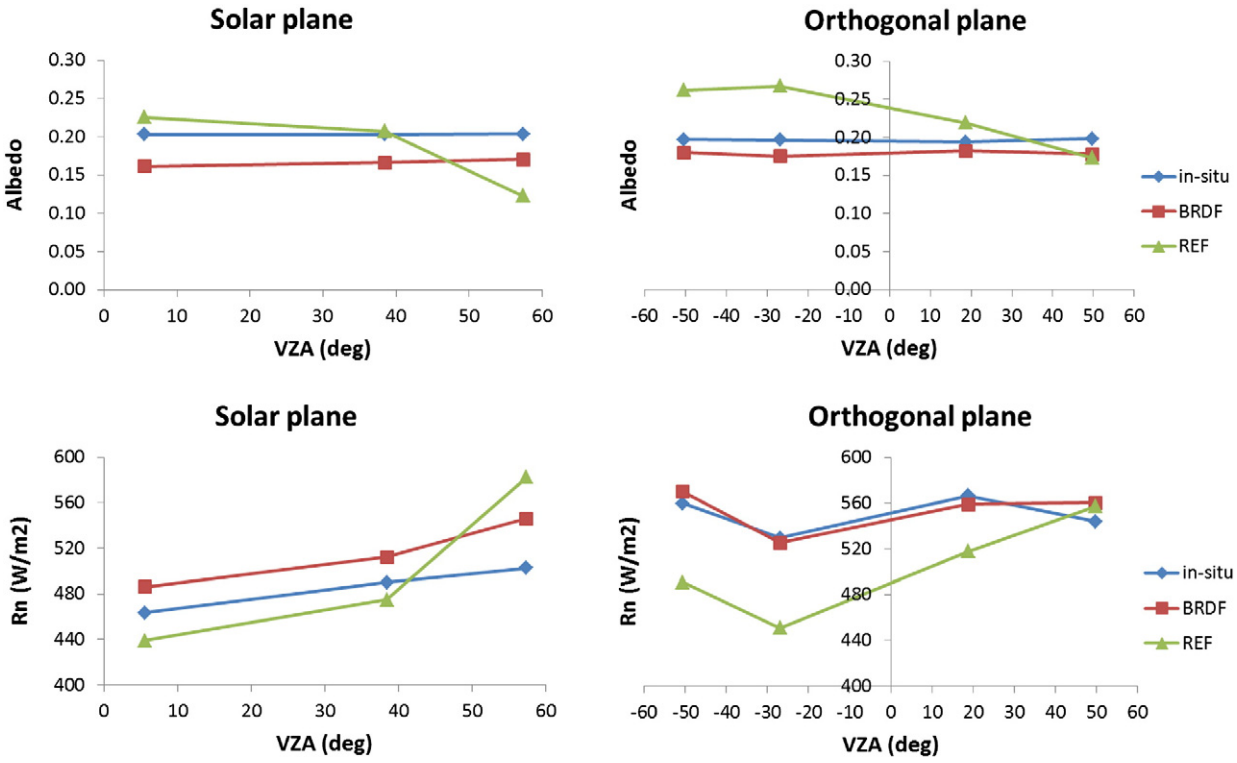

Fig. 13. Barley field surface broadband albedo and net radiation (W m^{-2}) time series comparison for each VZA differing between solar and orthogonal planes.

and estimates have been extensively validated at field scale using point measurements. However, the basin scale validations have not been extensively performed because the advances in estimating ET accurately at the basin or region scale (for validation) are still rather limited (Oudin et al., 2005). The results presented in this paper can be useful for local field experiment where high resolution hyperspectral images are involved. Indeed, the aggregation or disaggregation procedure may be influenced when using ASTER or Landsat images, where the surface broadband albedo was computed to estimate the evaporative or radiative regime. In these cases, the surface broadband albedo will separate the S-SEBI diagram and therefore the evapotranspiration value will be differentiated. On the other hand,

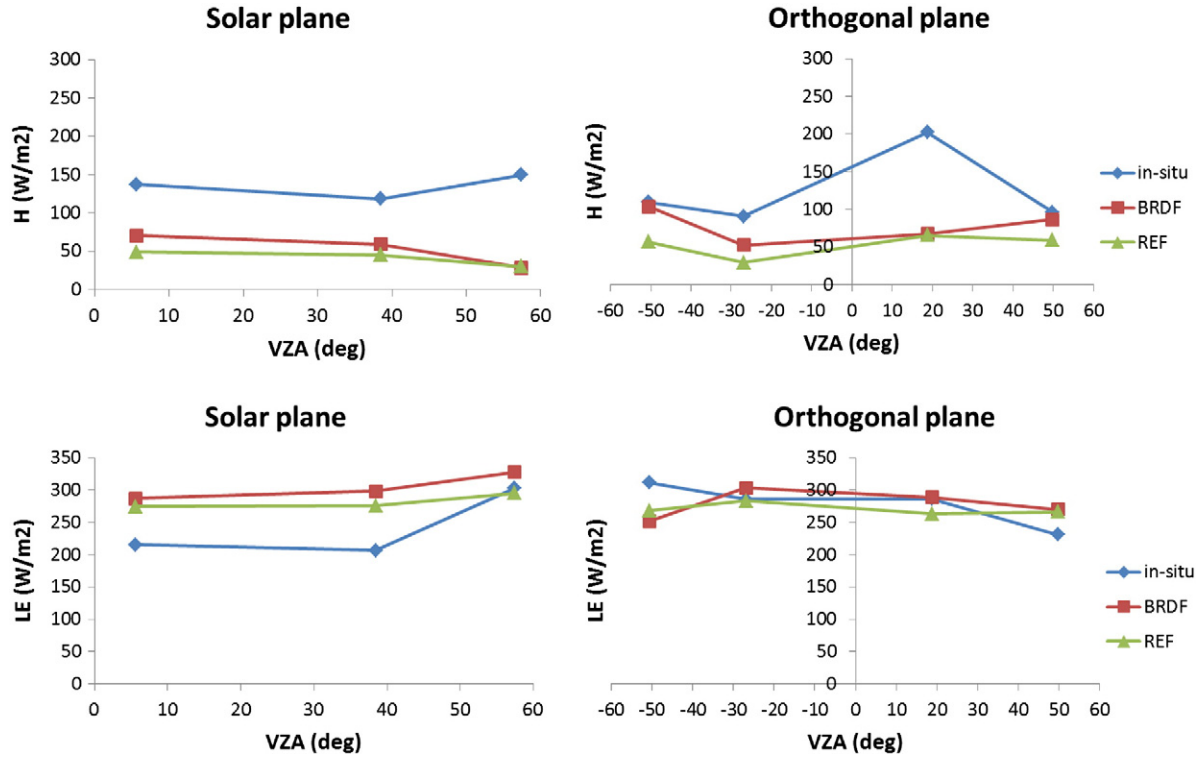

Fig. 14. Barley field sensible heat flux (W m^{-2}) and latent heat flux (W m^{-2}) time series comparison for each VZA differing between solar and orthogonal planes.

Table 8
Error analysis assuming *Rg*, *Tair* and *Cdi* invariant magnitudes.

		Albedo [−]	Rnet [W m^{-2}]	G [W m^{-2}]	*EF* [−]	LET [W m^{-2}]	ET_dia [mm d^{-1}]
Low	Absolute Values	0.165	689	178	0.567	290	4.34
	Absolute Errors	0.035	33.6	9.2	0.050	39.3	0.59
	Relative Errors [%]	21.4%	4.9%	5.1%	8.8%	13.6%	13.6%
Medium	Absolute Values	0.165	689	178	0.567	290	4.34
	Absolute Errors	0.072	68.0	18.2	0.088	72.9	1.10
	Relative Errors [%]	43.3%	9.9%	10.2%	15.4%	25.2%	25.3%
High	Absolute Values	0.165	689	178	0.567	290	4.34
	Absolute Errors	0.108	102.3	27.3	0.125	106.6	1.60
	Relative Errors [%]	65.2%	14.8%	15.3%	22.1%	36.8%	36.9%

for the case of MODIS, the basin scale can avoid the influences of the broadband albedo in the S-SEBI model. So, the applicability of this work to basin scale estimation is limited to whether physical downscaling methods are not applied.

Finally, angular effects on emissivity and/or LST can induce a possible bias in the S-SEBI diagram. In this work normalization of view angle effects on these two parameters was not considered, and TES retrievals refer to the value for a given pixel view angle. On the other hand, the emissivity term involved in the net radiation estimation (Eqs. (8) and (9)) is a broadband and hemispherical term, whereas in this paper a simple mean emissivity (averaged band surface emissivities) with no hemispherical integration was used. Analysis of angular effects on LST/emissivity and possible impacts on ET retrieval using the S-SEBI method requires further research. However, it is expected that these angular effects have a low impact on the ET retrieval, at least using the S-SEBI method and in comparison to the angular effects on surface albedo. For example, angular measurements carried out over the Barrax test site show an angular variation between nadir and 50° over bare soil of 0.7% (Cuenca & Sobrino, 2004), whereas angular variations estimated with a variety of directional models for mixed surfaces (soil and vegetation) are even lower, especially for surfaces with high Leaf Area Index (LAI) or Fractional Vegetation Cover (FVC) values (Sobrino, Jiménez-Muñoz, et al., 2005).

8. Conclusion

In this work, the angular influences on surface fluxes have been assessed. Using angular airborne images, the surface broadband albedo was retrieved by BRDF integration and by using the approximation of the equivalence to surface reflectance. The influence on the surface albedo was revealed for angles greater than 40°. Based on in-situ comparison, the surface reflectance approximation showed values even three times higher than the surface albedo derived from BRDF integration. The sensible heat flux, the latent heat flux and the daily evapotranspiration showed relative errors ranging between 23–39%, 6–18% and 5–15% respectively. Using the surface albedo instead of the surface reflectance improves the estimation of other flux variables such as net radiation, sensible and latent flux, evaporative fraction and it even affects the scatter distribution in the S-SEBI algorithm. Further studies are necessary to accuracy of S-SEBI for estimating daily evapotranspiration over other land surface covers by using different methods to estimate the surface albedo using BRDF methods. In a second part of this study, we will address the angular effects on surface emissivity with a focus on the implications for ET retrieval using the S-SEBI algorithm.

Acknowledgments

We acknowledge funding from the European Union (CEOP-AEGIS, project FP7-ENV-2007-1 Proposal No. 212921) and the Ministerio de Economía y Competitividad (EODIX, project AYA2008-0595-C04-01; CEOS-Spain, project AYA2011-29334-C02-01. This work was also partially funded by Program U-INICIA VID 2012, grant U-INICIA 4/0612; Santander Fellowship—University of Chile for young scientist and Fondecyt-Initial (CONICYT/ref-11130359).

References

Allen, R., Tasumi, M., & Trezza, R. (2007). Satellite-based energy balance for mapping evapotranspiration with internalized calibration METRIC—Model. *Journal of Irrigation and Drainage Engineering*, *133*(4), 380–394.
Bacour, C., & Breon, F. M. (2005). Variability of biome reflectance directional signatures as seen by POLDER. *Remote Sensing of Environment*, *98*, 80–95.
Bastiaanssen, W. G. M., Menenti, M., Feddes, R. A., & Holtslag, A. A. (1998). A remote sensing surface energy balance algorithm for land (SEBAL). 1 Formulation. *Journal of Hydrology*, *212–213*, 198–212.
Bastiaanssen, W. G. M. (2000). SEBAL-based sensible and latent heat fluxes in the irrigated Gediz Basin, Turkey. *Journal of Hydrology*, *229*, 87–100.
Berk, A., Anderson, G. P., Acharya, P. K., Chetwynd, J. H., Bernstein, L. S., Shettle, E. P., et al. (1999). *MODTRAN4 User's Manual*. Hanscom AFB, MA: Air Force Research Laboratory.
Bonan, G. B. (2008). Forests and climate change: Forcings, feedbacks, and the climate benefits of forests. *Science*, *320*, 1444–1449.
Breon, F. M., Maignan, F., Leroy, M., & Grant, I. (2002). Analysis of hot spot directional signatures measured from space. *Journal of Geophysical Research*, *107*(no. D16), 4282 (Aug. 22).
Cescatti, A., Marcolla, B., Santhana Vannan, S., Pan, J. Y., Román, M., Yang, X., et al. (2012). Intercomparison of MODIS albedo retrievals and in situ measurements across the global FLUXNET network. *Remote Sensing of Environment*, *121*, 323–324.
Chapin, F. S., Randerson, J. T., McGuire, A.D., Foley, J. A., & Field, C. B. (2008). Changing feedbacks in the climate–biosphere system. *Frontiers in Ecology and the Environment*, *6*, 313–320.
Chen, Y. M., Liang, S., Wang, J., Kim, H. Y., & Martonchik, J. V. (2008). Validation of MISR land surface broadband albedo. *International Journal of Remote Sensing*, *29*, 6971–6983.
Clothier, B. E., Clawson, K. L., Pinter, P. J., Jr., Moran, M. S., Reginato, R. J., & Jackson, R. D. (1986). Estimation of soil heat flux from net radiation and soil heat flux. *Remote Sensing of Environment*, *37*(3), 19–329.
Corbari, C., Ravazzani, G., & Mancini, M. (2011). A distributed thermodynamic model for energy and mass balance computation: FEST-EWB. *Hydrological Processes*, *25*, 1443–1452.
Corbari, C., Masseroni, D., & Mancini, M. (2012). Effetto delle correzioni dei dati misurati da stazioni eddy covariance sulla stima dei flussi evapotraspirativi. *Italian Journal of Agrometeorology*, *1*, 35–51.
Courault, D., Seguin, B., & Olioso, A. (2005). Review on estimation of evapotranspiration from remote sensing data: From empirical to numerical modeling approaches. *Irrigation and Drainage Systems*, *19*, 223–249.
Cuenca, C., & Sobrino, J. A. (2004). Experimental measurements for studying angular and spectral variation of thermal infrared emissivity. *Applied Optics*, *43*(23), 4598–4602.
Detto, M., Montaldo, N., Alberston, J., Mancini, M., & Katul, G. (2006). Soil moisture and vegetation controls on evapotranspiration in a heterogeneus Mediterranean ecosystem on Sardinia, Italy. *Water Resources Research*, *42*, 1–16.
Dickinson, R. E. (1983). Land surface processes and climate surface albedos and energy balance. *Advances in Geophysics*, *25*, 305–353.
Diner, D. J. (1999). *Level 2 surface retrieval algorithm theoretical basis document*. NASA/JPL, JPL D-11401, Rev. D.
Franch, B., Vermote, E. F., Sobrino, J. A., & Fédèle, E. (2013). Analysis of directional effects on atmospheric correction. *Remote Sensing of Environment*, *128*, 276–288.
French, A., Jacob, F., Anderson, M., Kustas, W., Timmermans, W., Gieske, A., et al. (2005). Surface energy fluxes with the Advanced Spaceborne Thermal Emission and Reflection radiometer (ASTER) at the Iowa 2002 SMACEX site (USA). *Remote Sensing of Environment*, *99*(1–2), 55–65.
Galleguillos, M., Jacob, F., Prévot, L., French, A., & Lagacherie, P. (2011). Comparison of two temperature differencing methods to estimate daily evapotranspiration over a Mediterranean vineyard watershed from ASTER data. *Remote Sensing of Environment*, *115*, 1326–1340.
Geiger, B., Carrer, D., Franchisteguy, L., Roujean, J. L., & Meurey, C. (2008). Land surface albedo derived on a daily basis from Meteosat Second Generation observations. *IEEE Transactions on Geoscience and Remote Sensing*, *46*, 3841–3856.

Gillespie, A., Rokugawa, S., Matsunaga, T., Cothern, J. S., Hook, S., & Khale, A. B. (1998). A temperature and emissivity separation algorithm for advance spaceborne thermal emission and reflection radiometer (ASTER) images. *IEEE Transactions on Geoscience and Remote Sensing*, *36*, 1113–1126.

Gomez, M., Olioso, A., Sobrino, J. A., & Jacob, F. (2005). Retrieval of evapotranspiration over the Alpilles/ReSeDA experimental site using airborne POLDER sensor and a thermal camera. *Remote Sensing of Environment*, *96*, 399–408.

Gowda, Chavez, P. J., Colaizzi, P., Evett, S., Howell, T., & Tolk, J. (2008). ET mapping for agricultural water management: present status and challenges. *Irrigation Science*, *26*(3), 223–237.

Gutman, G. G. (1991). Vegetation indices from AVHRR data: an update and future prospects. *Remote Sensing of Environment*, *35*, 121–136.

He, T., Liang, S., Wang, D., Wu, H., Yu, Y., & Wang, J. (2012). Estimation of surface albedo and directional reflectance from Moderate Resolution Imaging Spectroradiometer (MODIS) observations. *Remote Sensing of Environment*, *119*, 286–300.

Hsieh, C., Katul, G., & Chi, T. (2000). An approximate analytical model for footprint estimation of scalar fluxes in thermally stratified atmospheric flows. *Advances in Water Resources*, *23*, 765–772.

Jiménez-Muñoz, J. C., & Sobrino, J. A. (2006). Emissivity spectra obtained from field and laboratory measurements using the temperature and emissivity separation algorithm. *Journal of Applied Optics*, *45*(27), 7104–7109.

Jin, Y. F., Schaaf, C. B., Gao, F., Li, X. W., Strahler, A. H., Lucht, W., et al. (2003). Consistency of MODIS surface bidirectional reflectance distribution function and albedoretrievals: 1. Algorithm performance. *Journal of Geophysical Research-Atmospheres*, *108*, http://dx.doi.org/10.1029/2002jd002803.

Jin, Y., Schaaf, C. B., Woodcock, C. E., Gao, F., Li, X., Strahler, A. H., et al. (2003). Consistency of MODIS surface bidirectional reflectance distribution function and albedo retrievals: 2 Validation. *Journal of Geophysical Research*, *108*.

Kalma, J.D., McVicar, T. R., & McCabe, M. F. (2008). Estimating land surface evaporation: A review of methods using remotely sensed surface temperature data. *Surveys in Geophysics*, http://dx.doi.org/10.1007/s10712-008-9037-z.

Kljun, N., Calanca, P., Rotach, M., & Schmid, H. (2004). A simple parameterization flux footprint predictions. *Boundary-Layer Meteorology*, *112*, 503–523.

Kriebel, K. T. (1978). Measured spectral bidirectional reflection properties of 4 vegetated surfaces. *Applied Optics*, *17*, 253–259.

Lawrence, D.M., & Slingo, J. M. (2004). An annual cycle of vegetation in a GCM. Part II: Global impacts on climate and hydrology. *Climate Dynamics*, *22*, 107–122.

Leroy, M., Deuzé, J. L., Bréon, F. M., Hautecoeur, O., Hermann, M., Buriez, J. C., et al. (1997). Retrieval of atmospheric properties and surface bidirectional reflectances over land from POLDER/ADEOS. *Journal of Geophysical Research-Atmospheres*, *102*, 17023–17037.

Li, X., & Strahler, A. H. (1992). Geometric–optical bidirectional reflectance modelling of the discrete crown vegetation canopy: Effect of crown shape and mutual shadowing. *IEEE Transactions on Geoscience and Remote Sensing*, *30*, 276–292.

Liang, S. (2001). Narrowband to broadband conversions of land surface albedo: I. Formulae. *Remote Sensing of Environment*, *76*, 213–238.

Liang, S. L., Fang, H. L., Chen, M. Z., Shuey, C. J., Walthall, C., Daughtry, C., et al. (2002). Validating MODIS land surface reflectance and albedo products: Methods and preliminary results. *Remote Sensing of Environment*, *83*, 149–162.

Liang, S., Li, X., & Wang, J. (2012). *Broad-band albedo in advanced remote sensing.* Ed. AP—Elsevier.

Liu, H., Peters, G., & Foken, T. (2001). New equations for sonic temperature variance and buoyancy heat flux with an omnidirectional sonic anemometer. *Boundary-Layer Meteorology*, *100*, 459–468.

Liu, J., Schaaf, C., Strahler, A., Jiao, Z., Shuai, Y., Zhang, Q., et al. (2009). Validation of Moderate Resolution Imaging Spectroradiometer (MODIS) albedo retrieval algorithm: Dependence of albedo on solar zenith angle. *Journal of Geophysical Research*, *114*, D01106.

Lucht, W. (1998). Expected retrieval accuracies of bidirectional reflectance and albedo from EOS-MODIS and MISR angular sampling. *Journal of Geophysical Research*, *103*, 8763–8778.

Ma, W., Ma, Y., Li, M., Hu, Z., Zhong, L., Su, Z., et al. (2008). Estimating surface fluxes over the north Tibetan Plateau area with ASTER imagery. *Hydrology and Earth System Sciences Discussions*, *5*, 1705–1730.

Maignan, F., Breon, F. M., & Lacaze, R. (2004). Bidirectional reflectance of Earth targets: Evaluation of analytical models using a large set of space-borne measurements with emphasis on Hot-Spot. *Remote Sensing of Environment*, *90*, 210–220.

Massman, W. J., & Lee, X. (2002). Eddy covariance flux corrections and uncertainties in long-term studies of carbon and energy exchanges. *Agric For Meteorol*, *113*, 121–144.

McCabe, M. F., & Wood, E. F. (2006). Scale influences on the remote estimation of evapotranspiration using multiple satellite sensors. *Remote Sensing of Environment*, *105*, 271–285.

Menenti, M., & Choudhury, B. (1993). Parameterization of land surface evaporation by means of location dependent potential evaporation and surface temperature range. *Proceedings of IAHS conference on Land Surface Processes*, *212*. (pp. 561–568). IAHS Publ.

Nobre, C. A., Sellers, P. J., & Shukla, J. (1991). Amazonian deforestation and regional climate change. *Journal of Climate*, *4*, 957–988.

Oudin, L., Hervieu, F., Michel, C., Perrin, C., Andréassian, V., Anctil, F., & Loumagne, C. (2005). Which potential evapotranspiration input for a rainfall-runoff model? Part 2 - Towards a simple and efficient PE model for rainfall-runoff modelling. *Journal of Hydrology*, *303*(1-4), 290–306.

Ollinger, S. V., Richardson, A.D., Martin, M. E., Hollinger, D. Y., Frolking, S. E., Reich, P. B., et al. (2008). Canopy nitrogen, carbon assimilation, and albedo in temperate and boreal forests: Functional relations and potential climate feedbacks. *Proceedings of the National Academy of Sciences of the United States of America*, *105*, 19336–19341.

Payero, J. O., Neale, C. M. U., & Wright, J. L. (2005). Estimating soil heat flux for alfalfa and clipped tall fescue grass. *American Society of Agricultural Engineers*, *Vol. 21*(3), 401–409.

Payan, A., & Royer, A. (2004). Analysis of Temperature and Emissivity Separation (TES) algorithm applicability and sensitivity. *International Journal of Remote Sensing*, *25*(1), 15–37.

Pinty, B., & Verstraete, M. (1992). On the design and validation of surface bidirectional reflectance and albedo model. *Remote Sensing of Environment*, *41*, 155–167.

Pinty, B., Roveda, F., Verstraete, M., Gobron, N., Govaerts, Y., Martonchik, J., et al. (2000). Surface albedo retrieval from Meteosat—1. Theory. *Journal of Geophysical Research-Atmospheres*, *105*, 18099–18112.

Pinty, B., Taberner, M., Haemmerle, V. R., Paradise, S. R., Vermote, E., Verstraete, M., et al. (2011). Global-scale comparison of MISR and MODIS land surface albedos. *Journal of Climate*, *24*, 732–749.

Roerink, G. J., Su, B., & Menenti, M. (2000). S-SEBI: A simple remote sensing algorithm to estimate the surface energy balance. *Physics and Chemistry of the Earth, Part B*, *25*(2), 147–157.

Román, M.O., Schaaf, C. B., Lewis, P., Gao, F., Anderson, G. P., Privette, J. L., et al. (2010). Assessing the coupling between surface albedo derived from MODIS and the fraction of diffuse skylight over spatially-characterized landscapes. *Remote Sensing of Environment*, *114*, 738–760.

Román, M.O., Schaaf, C. B., Woodcock, C. E., Strahler, A. H., Yang, X., Braswell, R. H., et al. (2009). The MODIS (Collection V005) BRDF/albedo product: Assessment of spatial representativeness over forested landscapes. *Remote Sensing of Environment*, *113*, 2476–2498.

Roujean, J. -L., Leroy, M., & Deschamps, P. Y. (1992). A bidirectional reflectance model of the Earth's surface for the correction of remote sensing data. *Journal of Geophysical Research*, *97*, 20455–20468.

Roy, D. P., Lewis, P. E., & Justice, C. O. (2002). Burned area mapping using multi-temporal moderate spatial resolution data—A bi-directional reflectance model-based expectation approach. *Remote Sensing of Environment*, *83*(1/2), 263–286.

Ruhoff, A., Paz, A.R., Collischonn, W., Aragao, L., Rocha, H., & Malhi, Y. (2012). A MODIS-based energy balance to estimate evapotranspiration for clear-sky days in Brazilian tropical savannas. *Remote Sensing*, *4*, 703–725.

Samani, Z., Salim-Bawazi, A., Bleiweiss, M., Skaggs, R., & Tran, V. (2007). Estimating daily net radiation over vegetation canopy through remote sensing and climatic data. *Journal of Irrigation and Drainage Engineering*, *133*(4), 291–297.

Sauer, T. J., Meeka, D. W., Ochsnerb, T. E., Harrisc, A. R., & Hortond, R. (2003). Harrisc and R. Hortond, Errors in Heat Flux Measurement by Flux Plates of Contrasting Design and Thermal Conductivity. *Vadose zone Journal*, *2*(4), 580–588.

Schaaf, C. B., Gao, F., Strahler, A., Lucht, W., Li, X., Tsang, T., et al. (2002). First operational BRDF, albedo nadir reflectance products from MODIS. *Remote Sensing of Environment*, *83*, 135–148.

Schmid, H. (1994). Source areas for scalars and scalar fluxes. *Boundary-Layer Meteorology*, *67*, 293–318.

Sellers, P. J., Meeson, B. W., Hall, F. G., Asrar, G., Murphy, R. E., Schiffer, et al. (1995). Remote sensing of the land surface for studies of global change—Models, algorithms, experiments. *Remote Sensing of Environment*, *51*, 3–26.

Sellers, P. J., Fores, H., Kelly, R., Black, A., Baldocchi, D., Berry, J., et al. (1997). BOREAS in 1997: Experiment overview, scientific results, and future directions. *Journal of Geophysical Research-Atmospheres*, *102*, 28731–28769.

Seguin, B., & Itier, B. (1983). Using midday surface temperature to estimate daily evaporation from satellite thermal IR data. *International Journal of Remote Sensing*, *4*(2), 371–383.

Sobrino, J. A., Gómez, M., Jiménez-Muñoz, J. C., Olioso, A., & Chehbouni, A. (2005). *Journal of Hidrology*, *315*, 117–125.

Sobrino, J. A., Jiménez-Muñoz, J. C., & Verhoef, W. (2005). Canopy directional emissivity: Comparison between models, *99*(3), 304–314.

Sobrino, J. A., Jiménez-Muñoz, J. C., Zarco-Tejada, P. J., Sepulcre-Cantó, G., & de Miguel, E. (2006). Land surface temperature derived from airborne hyperspectral scanner thermal infrared data. *Remote Sensing of Environment*, *102*, 99–115.

Sobrino, J., Gomez, M., Jimenez-Munoz, J., & Olioso, A. (2007). Application of a simple algorithm to estimate daily evapotranspiration from NOAA-AVHRR images for the Iberian Peninsula. *Remote Sensing of Environment*, *110*(2), 139–148.

Sobrino, J. A., Jimenez-Munoz, J. C., Balick, L., Gillespie, A.R., Sabol, D. E., & Gustafson, W. T. (2007). Accuracy of ASTER level-2 thermal-infrared standard products of an agricultural area in Spain. *Remote Sensing of Environment*, *106*, 146–153.

Sobrino, J. A., Jiménez-Muñoz, J. C., Sòria, G., Gòmez, M., Barella Ortiz, A., Romaguera, M., et al. (2008). Thermal remote sensing in the framework of the SEN2FLEX project: Field measurements, airborne data and applications. *International Journal of Remote Sensing*, *29*(17–18), 4961–4991.

Sobrino, J. A., Jiménez-Muñoz, J. C., Zarco-Tejeda, P., Sepulcre-Cantó, G., de Miguel, E., Sòria, G., et al. (2009). Thermal Remote Sensing fromAirborne Hyperspectral Scanner data in the framework of the SPARC and SEN2FLEX projects: An overview. *Hydrology and Earth System Sciences*, *13*, 2031–2037.

Sobrino, J. A., Mattar, C., Gastellu-Etchegorry, Jiménez-Muñoz, J. C., & Grau, E. (2011). Evaluation of the DART 3D model in the thermal domain using satellite/airborne imagery and ground-based measurements. *International Journal of Remote Sensing*, *32*(22), 7453–7477.

Sobrino, J. A., Franch, B., Mattar, C., Jiménez-Muñoz, J. C., & Corbari, C. (2012). A method to estimate soil moisture from Airborne Hysperspectral Scanner (AHS) and ASTER data: Application to SEN2FLEX and SEN3EXP campaigns. *Remote Sensing of Environment*, *17*, 415–428.

Sobrino, J. A., Franch, B., Oltra-Carrió, R., Vermote, E. F., & Fedele, E. (2013). Evaluation of the MODIS Albedo product over a heterogeneous agricultural area. *International Journal of Remote Sensing*, *34*(15), 5530–5540.

Strahler, A. H., Lucht, W., Schaaf, C. B., Tsang, T., Gao, F., Li, X., et al. (1999). *MODIS BRDF albedo product: Algorithm theoretical basis document, NASA EOS-MODIS Doc., V5.0.*

Strugnell, N. C., & Lucht, W. (2001). An algorithm to infer continental-scale albedo from AVHRR data, land cover class, and field observations of typical BRDFs. *Journal of Climate*, *14*, 1360–1376.

Su, Z. (2002). The surface energy balance system (SEBS) for estimation of turbulent heat fluxes. *Hydrology and Earth System Sciences*, *6*(1), 85–99.

Su, Z. H., Pelgrum, & Menenti, M. (1999). Aggregation effects of surface heterogeneity in land surface processes. *Hydrological and Earth System Sciences*, *3*(4), 549–563.

Timmermans, W., Kustas, W., Anderson, M., & French, A. (2007). An intercomparison of the Surface Energy Balance Algorithm for Land (SEBAL) and the Two-Source Energy Balance (TSEB) modeling schemes. *Remote Sensing of Environment*, *108*(4), 369–384.

Tittebrand, A., & Berger, F. (2008). Spatial heterogeneity of satellite derived land surface parameters and energy flux densities for LITFASS-area. *Atmospheric Chemistry and Physics Discussion*, *8*(4), 16219–16254.

Tanner, C., & Thurtell, G. (1969). *Anemoclinometer measurements of Reynolds stress and heat transport in the atmospheric surface layer.* ECOM 66-G22-F, ECOM, United States Army Electronics Command, Research and Development.

Velpuri, N. M., Senay, G. R., Singh, R. K., Bohms, S., & Verdin, J. P. (2013). A comprehensive evaluation of two MODIS evapotranspiration products over the conterminous United States: Using point and gridded FLUXNET and water balance ET. *Remote Sensing of Environment*, *139*, 35–49.

Vermote, E., Tanré, D., Deuzé, J. L., Herman, M., & Morcrette, J. J. (1997). Second simulation of the satellite signal in solar spectrum: An overview. *IEEE Transactions on Geoscience and Remote Sensing*, *35*, 675–686.

Verstraeten, W. W., Veroustraete, F., & Feyen, J. (2005). Estimating evapotranspiration of European forests from NOAA-imagery at satellite overpass time: Towards an operational processing chain for integrated optical and thermal sensor data products. *Remote Sensing of Environment*, *96*, 256–276.

Vermote, E. F., & Roy, D. P. (2002). Land surface hotspot observed by MODIS over central Africa. *International Journal of Remote Sensing*, *23*, 2141–2143.

Vinukollu, R., Wood, E., Ferguson, C., & Fisher, J. (2011). Global estimates of evapotranspiration for climate studies using multi-sensor remote sensing data: Evaluation of three process-based approaches. *Remote Sensing of Environment*, *115*(3), 801–823.

Wang, K., Liang, S., Schaaf, C. L., & Strahler, A. H. (2010). Evaluation of Moderate Resolution Imaging Spectroradiometer land surface visible and shortwave albedo products at FLUXNET sites. *Journal of Geophysical Research*, *115*, D17107.

Webb, E., Pearman, G., & Leuning, R. (1980). Correction of the flux measurements for density effects due to heat and water vapour transfer. *Boundary-Layer Meteorology*, *23*, 251–254.